Modelling of High-energy Radiation Damage in Materials relevant to Nuclear and Fusion Energy

by

Evangelia Zarkadoula

A thesis submitted to the University of London for the degree of
Doctor of Philosophy

School of Physics and Astronomy
Queen Mary, University of London
United Kingdom

August 2013

To my parents Maria and Nikos,
and my siblings Vasia & Panagiotis (and their little Maria), Thanasis, and Nikoleta for believing in me.

To Roy, for keeping me on the right path.

Abstract

The objective through my PhD has been to investigate radiation damage effects in materials related to fusion and to safe encapsulation of nuclear waste, using Molecular Dynamics (MD) methods. Particularly, using MD, we acquire essential information about the multi-scale phenomena that take place during irradiation of materials, and gain access at length and time-scales not possible to access experimentally. Computer simulations provide information at the microscopic level, acting as a bridge to the experimental observations and giving insights into processes that take place at small time and length-scales. The increasing computer capabilities in combination with recently developed scalable codes, and the availability of realistic potentials set the stage to perform large scale simulations, approaching phenomena that take place at the atomistic and mesoscopic scale (fractions of μm for the first time) in a more realistic way. High-energy radiation damage effects have not been studied previously, yet it is important to simulate and reveal information about the properties of the materials under extreme irradiation conditions. Large scale MD simulations provide a detailed description of microstructural changes. Understanding of the primary stage of damage and short term annealing (scale of tens of picoseconds) will lead to better understanding of the materials properties, best possible long-term use of the materials and, importantly, new routes of optimization of their use. Systems of interest in my research are candidate fusion reactor structural materials (iron and tungsten) and materials related to the radioactive waste management (zirconia). High-energy events require large simulation box length in order for the damage to be contained in the system. This was a limitation for previous simulations, which was recently shifted with my radiation damage MD simulations. For the first time high-energy radiation damage effects were simulated, approaching new energy and length scales, giving a more realistic view of processes related to fusion and to high-energy ion irradiation of materials.

Acknowledgments

First of all, I would like to express my deepest respect and gratitude to my supervisor and mentor Dr Kostya Trachenko for always supporting me. This three-year journey would not have been the same without his guidance.

I am particularly grateful to our collaborators from Daresbury Laboratory Dr Ilian Todorov and Dr Michael Seaton, for all of their priceless help and to Prof Martin Dove, head of our group in Queen Mary, for his significant involvement in this work. I would like to thank my collaborators from UCL, Dr Dorothy Duffy and Szymon Daraszewicz, Prof Kai Nordlund from Helsinki University, Prof William Weber from Oak Ridge National Laboratory, Dr Ram Devanathan from Pacific Northwest National Laboratory. Many thanks to Dr Ewan Maddrell from National Nuclear Laboratory for useful discussions. I would also like to especially thank Predrag Micakovic and Sarah Cowls from our School in Queen Mary, for always being so helpful and kind.

I am grateful to South East Physics network (SEPnet) for funding this project. I would also like to deeply thank the HPC Materials Chemistry Consortium, chaired by Prof Richard Catlow, through which I have been allocated millions of computational allocation units in order to accomplish this task. Without their support none of this would have been possible.

I am grateful to my family for always believing in me, and to my friends that did not let the distance separate us. I deeply thank all these people that supported my efforts and dreams in the last three years. I thank Roy especially, for believing in me and supporting me.

Table of Contents

List of Figures

List of Tables

List of Abbreviations

2T-MD	Two-Temperature Model
AUs	(time) Allocation Units
e-p	electron-phonon
EAM	Embedded Atom Method
EEL	Electronic Energy Loss
EPSRC	Engineering and Physical Sciences Research Council
FD	Finite Difference
FP	Frenkel Pair
MD	Molecular Dynamics
N_{def}	Number of defect atoms
N_{disp}	Number of displaced atoms
nn	nearest neighbour
NPT	constant pressure and temperature ensemble
NVE	microcanonical ensemble
NVT	constant volume ensemble
PBC	Periodic Boundary Conditions
PKA	Primary Knock-on Atom
RDF	Radial Distribution Function
SIA	Self-Interstitial Atom

TEM	Transmission Electron Microscopy
V-I	Vacancy-Interstitial
ZBL	Ziegler-Biersack-Littmark potential
τ_{def}	Relaxation time corresponding to the width of the peak of the defect atoms
τ_{disp}	Relaxation time corresponding to the width of the peak of the displaced atoms

Chapter 1

Introduction and Outline of the Project

1.1 Intoduction

Radiation effects are common in nature. Their sources vary from cosmic radiation to decay of isotopes in terrestrial rocks. Radiation effects have been finding increasing applications in various fields with notable examples of the semiconductor and nuclear industries. In nuclear power applications materials will be exposed to high dose irradiation coming from highly energetic products of fission and fusion. In existing nuclear power stations kinetic energy of fission products is converted into heat and electricity. When feasible, future fusion reactors will harvest the energy from thermonuclear reactions. In these applications, the energy of emitted particles has a two-fold effect: on one hand, this energy is converted into useful energy, by heating the material; on the other hand, this energy damages the material and degrades the properties important for the operation of the nuclear reactors, including mechanical, thermal, transport and other properties. This is currently a central issue for fusion reactors, where the ability of metal structural components to withstand very high neutron fluxes and other types of radia-

tion such as He, is intensely discussed [1–3]. Another example is the damage of nuclear reactor materials due to fission products, such as heavy nuclei and neutrons, and due to alpha decay processes, where heavy radioactive nuclei and alpha particles are produced. In addition, the nuclear industry faces yet another problem, that of radiation damage in materials to be used to encapsulate long-lived radioactive waste [4–10]. Importantly, the public acceptance of nuclear power also depends on the ability of nuclear waste immobilization.

Radiation damage takes place when an energetic particle displaces atoms on its path which, in turn, displace other atoms in the system. A collection of these atoms is often referred to as a "collision cascade" [11–17]. A typical collision cascade created by a heavy 100 keV particle propagates and relaxes in some tens of picoseconds and spans nanometers. The resulting structural damage, in the form of amorphous pockets or point defects and their clusters, as well as their long-term evolution, ultimately define to what extent the materials' mechanical and thermal properties are altered. For example, radiation-induced defects and their structures can reduce the materials' thermal conductivity and therefore result in inefficient energy transfer in both fission and fusion reactors, heat localization and other unwanted effects, such as increased brittleness.

Candidate materials for safe encapsulation of nuclear waste need to be structurally stable and have low diffusion rates of radioactive ions to prevent polluting the environment. Waste forms often become amorphized by radiation damage from the radioactive nuclear waste, with most of amorphization produced by energetic heavy ions in collision cascades that consist of atoms displaced from their sites [4–6, 11]. Amorphization, described as loss of long–range order [18], can alter some of the materials properties, such as mechanical durability [19] and diffusion rate, which can be dramatically increased [6, 20]. For this reason, the search for radiation-resistant waste forms [7, 21]) has been on for several decades.

One of the properties related to radiation damage effects that is of great interest is the resistance to amorphization. Being able to predict the materials' resistance to

amorphization is essential in order to find suitable materials for nuclear waste storage and fusion applications. Another significant aspect for predicting the long–term behaviour of the materials is understanding radiation damage effects of plutonium disposition in potential waste matrices [22]. Overall, radiation damage effects cause alteration of the materials' properties and fundamental understanding of how this alteration affects the materials' performance is of great importance.

Understanding of significant and basic aspects of the interaction of radiation with solids, including radiation effects, defect investigation, ion-beam modification of materials, electronic and ionic transport, materials characterization, and predicting the materials' behaviour in intense radiation environments, requires the development of physical models [23]. Computer simulation is a modern tool to investigate such phenomena, and importantly, it is used to give insights into the microscopic level in a way that is not possible in experiments.

Molecular dynamics (MD) give access to the trajectory of the system in the phase space. In MD simulations the equations of motion $F = ma$ are solved numerically, providing a description of the system at any time. Therefore, MD modeling is an important method for studying radiation damage in materials, which gives access to the small time and length scales of the collision cascades, and gives a detailed description of the damage at the atomistic scale.

Previous MD simulations have provided important insights into the radiation damage process [11–17, 22, 24, 25]. However, due to system size limitations in MD simulations, the reported results were limited to energies of about 100 keV. The penetration path of a projectile increases with increasing energy and in order to contain a particle moving with velocity that corresponds to high energy in a MD simulation box, large system size is needed. Until recently the available computer facilities were limiting the simulations to small system sizes, so to lower energy events. Energies relevant to fission products and fusion have not been studied before, yet are important to simulate [2] and give us a more realistic view of the effects that high–energy irradiation has on matter. When

impacted on 14 MeV neutrons, iron knock-on atoms in fusion reactors reach energy of up to 1 MeV [2, 12, 26] with an average energy of about 0.5 MeV [24]. In fission nuclear reactions, the fission product energies are on the order of 50 to 100 MeV, transferring high energy to the surrounding material. The need to simulate realistic energy cascades has been particularly emphasized, with a view that extrapolation of low-energy results may not account for some important features of higher-energy radiation processes which can contain novel qualitative features [2]. More generally, the need to simulate length and energy scales that are relevant and appropriate to a particular physical process has been recognized and reiterated [27].

During my PhD, the box length limitation, and consequently the energy range limitation, was shifted for the first time. The combination of an almost perfectly scalable MD code, DLPOLY [28, 29] and the parallel supercomputing facilities of HECToR [30], on which we had access through the HPC Materials Chemistry Consortium, set the stage for simulations of energies related to fusion, in system sizes of $0.1 - 0.2$ μm. We carried out the largest simulations performed for systems with realistic interatomic potentials, using up to 65,000 cores for a single job. For the accomplishment of this project we used 217 million time allocation units (AUs) on HECToR which is equivalent to 54 million CPU hours. A generous discounted rate from HECToR lead to charge of 75 million AUs (19 million CPU hours). We simulated for the first time systems consisting of 150 million atoms using a many-body potential, while up to 1 billion atoms system can be simulated using a simple interatomic interaction (Lennard–Jones). We studied the effects of high–energy radiation damage in various systems related to nuclear power applications: α-iron and tungsten, in regard to structural materials for future fusion reactors, and zirconia, regarding the safe storage and immobilization of nuclear waste. We studied the damage creation, propagation and annihilation in the system, the morphology of high-energy collision cascades and the damage at local scale.

Throughout this PhD project, I pushed the boundaries of what has been thought to be possible in MD simulations, and have successfully exploited the combination of

massive parallel computer facilities and the MD package DLPOLY. For the accomplishment of these state-of-the-art simulations a lot of time and effort was invested in code development. The outputs of this work of a technical nature are beneficial for further development and performance of large scale modelling, not only in radiation damage, but in a wider scientific field. New challenges emerged during the performance of these large scale simulations related to the code's capabilities and efficiency, such as on-the-fly analysis (dynamic analysis of the simulation as it is being performed), radiation damage features implementation, testing new algorithms implemented for the accomplishment of this work and issues related to the large size of the files, including non-trivial input/output issues when 30,000-65,000 processors write to one file, challenges that we overcame in close collaboration with the code developing team. For instance, a configuration of 250 million atoms is about 100 Gb, meaning that a 10,000-frame history file is Petabyte in size. Writing a file of this size would - if it was even possible - require 80% of the computational time, making the simulation inefficient and resulting in a waste of computational time. This and other non anticipated issues that I flagged urged the need for on-the-fly analysis, modification of the code and further development of radiation damage features in the code that we implemented and tested as members of the developing team. Some of the modifications of the code are already included in the public version while others are under investigation and the features added will be included in the next versions of the code to be released.

Being actively involved in the development of the code and testing new features for large scale radiation damage simulations has been extremely challenging, yet it was gratifying to see that the outcomes have been fruitful not only for this work but also for a wider community interested in large-scale MD simulations. Indeed, new features related to very large sizes will be relevant in other areas, such as microcracks, biomolecules, protein folding, molecular assembly processes, grain boundaries and so on.

1.2 Outline

A short introduction to MD simulations is presented in **Chapter 2**, followed by the description of basic features applied in the simulations performed for this PhD project and a description of the code implementations and modifications we made in collaboration with the DLPOLY code development team.

In **Chapter 3** we study collision cascades in Fe due to high-energy Fe recoils carrying 200 - 500 keV energy, which was transferred to them from the high–energy neutrons produced in fusion. Bcc-iron is a compound metal of candidate bcc-materials to be used in fusion reactors. We simulate collision cascades for different directions of the recoil in a system consisting of about 100 million atoms. For these simulations, we take into account the electronic stopping mechanism, which is of great importance when energies of these scales are simulated, as the primary knock-on atoms (PKAs) lose a part of their energy due to the electrons of the system. We describe the large scale damage by describing the morphology of the cascade, and we discuss the damage annealing mechanisms. Defect analysis is summarized and new defect structures that have not been experimentally observed are presented.

In the following chapter (**Chapter 4**) we extend the high–energy collision cascade simulations in iron by implementing the full two temperature model (2T-MD) as described by Rutherford and Duffy [31, 32]. In this work, we implement the electron–phonon interaction, in addition to the electronic stopping effect, and we compare the outcomes of simulations with only the electronic friction mechanism switched on and with the full two temperature model applied. We discuss the effect of the electron–phonon interaction on the damage creation and annealing for cascades of 100 keV and 200 keV. We discuss the effect of the two mechanisms on the relaxation time of the cascades. Lastly, we provide the defect analysis and statistics for the simulations performed.

In **Chapter 5** we present our first findings on simulations in tungsten, a strong candidate structural material for future fusion reactors. We simulate W recoils of 300

keV energy, which is the maximum energy that can be transferred to an atom of the system from a 14 MeV neutron produced in fusion. We first study the effect of electron-phonon coupling on the damage creation and annihilation for different directions of the recoil in a system of about 30 million atoms. Second we perform simulations at 800 K, the fusion reactor's operating temperature, and study the effect of temperature on the damage evolution.

In **Chapter 6** we investigate high–energy radiation damage in cubic zirconia. Zirconia is a strong candidate material for nuclear waste matrices, as it is one of the most resistant to amorphization ceramics. We perform simulations of 100 keV uranium recoils, which are related to Pu doping experiments. We perform simulations for different directions of the recoil velocity with and without the effect of electronic energy loss and compare the results, highlighting the need to include the electronic stopping in high-energy collision cascades. Additionally, we simulate 300 and 500 keV collision cascades for different directions of the U recoils, events related to high–energy ion bombardment experiments. In these sets of simulations, we include the friction due to the electronic stopping. We provide the defect analysis for all performed cascades.

In the final chapter (**Chapter 7**) we summarize and conclude on the work presented.

References

[1] D. J. Ward and S. L. Dudarev, Materials Today, **11**, 46 (2008).

[2] A. M. Stoneham, J. R. Matthews and I. J. Ford, J. Phys.: Condens. Matter **16**, S2597 (2004).

[3] S. L. Dudarev, J-L. Boutard, R. Lasser, M. J. Caturla, P. M. Derlet, M. Fivel, C-C. Fu, M. Y. Lavrentiev, L. Malerba, M. Mrovec, D. Nguyen-Manh, K. Nordlund, M. Perlado, R. Schaublin, H. Van Swygenhoven, D. Terentyev, J. Wallenius, D. Weygand, W. Willaime, J. Nuclear Mater. **386**, 1 (2009).

[4] A. E. Ringwood, V.M. Oversby, S.E. Kesson, W. Sinclair, N. Ware, W. Hibberson,

and A. Major, Nuclear and Chemical Waste Management **2**, 287 (1981).

[5] W. J. Weber, R. C. Ewing, C. R. A. Catlow, T. Diaz de la Rubia, L. W. Hobbs, C. Kinoshita, Hj. Matzke, A. T. Motta, M. Nastasi, E. K. H. Salje, E. R. Vance and S. J. Zinklea, J. Mater. Res. **13**, 1434 (1998).

[6] T. Geisler, K. Trachenko, S. Rios, M. T. Dove, and E. K. H. Salje, J. Phys.: Condens. Matter **15**, L597 (2003).

[7] W. E. Lee, M. I. Ojovan, M. C. Stennett and N. C. Hyatt, Adv. Appl. Ceram. **105**, 3 (2006).

[8] P.A. Bingham, A.J. Connelly, N.J. Cassingham and N.C. Hyatt J. Non-Cryst. Solids **357**, 27262734 (2011).

[9] A. Covill, N. Hyatt, J. Hill, N. C Collier Adv. Appl. Ceram. **110**, 151-156 (2011).

[10] O.J. McGann, P.A. Bingham, R.J. Hand, A.S. Gandy, M. Kavcic, M. Zitnik, K. Bucar, R. Edge, N.C. Hyatt J. Nucl. Mater. **429**, 353367 (2012).

[11] R. S. Averback and T. Diaz de la Rubia, Solid State Physics (ed. H. Erhenfest and F. Spaepen, Academic Press, New York) **51**, 281 (1998).

[12] S. Ishino, P. Schiller and A. F. Rowcliffe, Journal of Fusion Energy **8**, 147 (1989).

[13] K. Nordlund, Nuclear Instr. Meth. Phys. Res. B **188**, 41 (2002).

[14] A. Souidi, C.S. Becquart, C. Domain, D. Terentyev, L. Malerba, A.F. Calder, D.J. Bacon, R.E. Stoller, Yu. N. Osetsky, and M. Hou, J. Nucl. Mater. **355**, 89 (2006).

[15] A. F. Calder, D. J. Bacon, A. V. Barashev and Y. N. Osetsky, J. Nucl. Mater. **382**, 91 (2008).

[16] K. Morishita and T. Diaz de la Rubia, J. Nucl. Mater. **271**, 35 (1999).

[17] D. J. Bacon, Yu. N Osetsky, R Stoller, and R.E Voskoboinikov, J. Nucl. Mater. **323**, 152 (2003).

[18] K. Trachenko, M. T. Dove, and E. Artacho, I. T. Todorov and W. Smith, Phys. Rev. B **73**, 174207 (2006).

[19] K. Trachenko, J. Phys.: Condens. Matt. **16**, R1491 (2004).

[20] K. Trachenko, M. T. Dove, T. Geisler, I. Todorov and B. Smith, J. Phys. Condens. Mat. **16**, S2623 (2004).

[21] P.A. Bingham, A.J. Connelly, R.J. Hand, and N.C. Hyatt, Nuclear Future **6**, 250-254

(2010).

[22] C. Davoisne, W. E. Lee, M. C. Stennett, N. C. Hyatt, N. Peng, C. Jeynes, Advances in Materials in Science for Environmental and Nuclear Technology (*Ceramic Transactions*) **222**, 3-9 (2010).

[23] C. R. A. Catlow, Curr. Opin. Solid State Mater. Sci. **7**, 1 (2003).

[24] R. E. Stoller and L. R. Greenwood, Journal of Nuclear Materials **271–272**, 57 (1999).

[25] A. F. Calder, D. J. Bacon, A. V. Barashev and Yu. N. Osetsky, Phil. Mag. **90**, 863 (2010).

[26] R. E. Stoller, Comprehensive Nuclear Materials **1**, 293 (2012) (Ed. R. J. M. Konings, Elsevier, Amsterdam, 2012).

[27] A. M. Stoneham and J. H. Harding, Nature Materials **2**, 77, (2003).

[28] I. T. Todorov, B. Smith, K. Trachenko and M. T. Dove, Capability Computing **6**, 12 (2005).

[29] I. T. Todorov, B. Smith, M. T. Dove and K. Trachenko, J. Mater. Chem. **16**, 1911 (2006).

[30] http://www.hector.ac.uk

[31] D. M. Duffy and A. M. Rutherford, J. Phys.: Condens. Mat. **19**, 016207 (2007).

[32] A. M. Rutherford and D. M. Duffy, J. Phys.: Condens. Mat. **19**, 496201 (2007).

Chapter 2

Methods

In this chapter we present a brief introduction to MD methods and provide a description of features applied in the simulations performed for this work.

2.1 Molecular Dynamics Simulations

MD technique solves Newton's law of motion $F = ma$ to calculate the trajectories of all particles in the system. From the trajectories of the atoms, the coordinates and velocities can be calculated and this way the state of the system can be predicted at any time. With the use of accurate force fields to describe the interactions between the atoms of the system and statistical mechanics, MD simulations provide information of the dynamics of the system at the microscopic level. The system is treated as a collection of different microscopic states but with an identical macroscopic state (ensemble).

MD methods were first introduced by Alder and Wainwright in 1957 [1] in order to describe the hard sphere interaction. The first MD simulation was performed in the 1960's by Rahman [2] on argon, and some years later Stillinger and Rahman carried out the first simulation in liquid water [3]. Following the field of physics, the first MD simulation in the field of biology was performed in the 1970's [4]. Radiation damage modeling

was first performed in the 1980's [5–7], followed by more detailed simulations of defects and displacements in the 1990's [8–13]. Since then, the evolution of computer facilities, and especially the recent breakthrough in high-performance computing in material science [14], has allowed MD simulations not only to explain experimental results, but also to predict them [15].

MD simulations have been used to study a plethora of phenomena taking place at the micro–level, such as diffusion [16, 17] , grain growth and grain boundaries [18, 19] and phase transitions [20–22]. MD require the use of accurate interatomic potentials to describe the forces between the atoms. These potentials are usually fitted to experimental values or *ab initio* calculations of the materials' properties and need to achieve accuracy and computational efficiency. Examples of such potentials for metals are the Finnis-Sinclair potential [23], Mendelev et al potential [24], Ackland et al potential [25] and Dudarev-Derlet potential [26], and modifications of them [27–30], in which the embedded atom method [31](EAM) potential was applied. Other examples include the Tersoff potential for silicon [32], Ferrari et al. potential for phase transitions in potassium tetrachlorozincate [33], a modification [34] of Fisler potential [35] for a range of carbonate structures, Schelling et al. [22] and Yu et al. [36] potentials for zirconia, and Mendelev and Ackland potential for phase transformations in zirconium [37].

Several codes using MD techniques, for example MOLDY, DYMOKA, LIVCAS, MDCASK, LAMMPS and DLPOLY, with the last two being perfectly scalable, meaning their ability to perform efficiently when the load increases (linear relationship between number of cores and efficiency, i.e. if you double the number of cores you double the efficiency), have been used for studying irradiation and its effects on metals, but these studies were limited to up to 100 keV energy, while the simulation box size was up to 1,000,000 atoms [27, 28, 38–42]. Displacement cascades in iron have been modeled before using MD techniques, but the simulation methods were limited to small box sizes and low energies in the range of some tens of keV [27, 38, 43, 44]. There is, however, still the need to further investigate more realistic energy (hundreds of keV up to 1MeV) and

length scales [45].

Previous work on radiation damage has shown that the damage recovery, and as a result the resistance to amorphization, is different in different materials [46]. There have been many theories and models proposed for explaining resistance to amorphization [46]. Based on extensive analysis of experimental data, theory and ab initio simulations [46, 47], it was proposed that the type of interaction and the nature of chemical bond play a crucial role in this process [48]. Increasing computing capabilities and development of more accurate interatomic potentials have resulted in better efficiency and accuracy of the MD codes. The fact that results gained from radiation damage modelling are in good agreement with experiment [49–51] implies that MD simulation can directly predict resistance to amorphization by radiation damage [46], predict experimental results and interpret experimental observations [15].

The progress made on code scalability, interatomic potential development and computer capabilities set the stage for high energy radiation damage simulations in large systems, up to 1 billion atoms.

2.2 Features

In this section we present features that have been applied to simulations performed in this work, including a brief description of the conditions in which we equilibrated the systems.

2.2.1 Ensembles

2.2.1.1 NVE

The microcanonical ensemble describes a system of constant number of particles N, constant volume V and constant energy E. NVE ensemble was applied to all the atoms

of the system, except for those contained in the boundary layer (see section 2.2.5), for the cascade simulations where the electronic effect mechanisms are not implemented.

2.2.1.2 NPT

We use the NPT ensemble in which the system is coupled to a Berendsen thermostat, an external bath with constant temperature and pressure [52]. The thermostat and barostat relaxation times are user adjustable. The equilibration of the systems (2.2.2) are performed in this ensemble.

2.2.1.3 NVT

The implementation of the electronic effects mechanisms (2.3.6) is done in the NVT ensemble, in which the volume is constant and the system is coupled to an inhomogeneous Langevin thermostat, which uses the local electronic temperature.

2.2.2 System equilibration

All systems are equilibrated in the NPT ensemble coupled to a Berendsen thermostat [52] for 3-7 ps, with a constant timestep of 0.001 ps. The system's temperature is rescaled after each step during equilibration. Following that, we allow the system to relax for 2-3 ps using the same timestep, until the atoms settle in their equilibrium positions.

2.2.3 Periodic Boundary Conditions

In our modeling of radiation damage effects we are interested in the bulk. In order to eliminate the surface effects, we use periodic boundary conditions (PBC), which replicate the initial MD cell towards all directions. This results in a system where all atoms are images of the atoms in the initial MD cell, with the total number of atoms in the

system being conserved. PBC enable the calculations to be performed from a small number of particles, increasing the calculation efficiency. We use an orthorhombic cell (orthorhombic periodic boundary conditions), as a more general case of cubic systems simulated here, with the cell defined with principle axes passing through the centers of the faces [53].

2.2.4 Variable timestep

For the simulations of the collision cascades we use variable timestep, which accounts for the different dynamics of the system during the cascade evolution. This is the only realistic approach as at the beginning of the simulation the atomic motion is fast due to the high energy of the atoms, when a small timestep is needed, while during the development of the cascade the atomic motion slows down, needing a larger value of timestep. A constant timestep, even a small value of it, would fail to describe the dynamics of system during the cascade evolution. The initial timestep can be of the order of 0.01 fs, reaching the order of 1 fs as the system relaxes.

2.2.5 Boundary Thermostat

In our simulations, a layer at the boundaries of the MD box is coupled to a constant temperature thermostat to emulate the effect of energy dissipation into the sample. Such treatment of the MD simulation box boundaries, where the velocity of atoms that are contained there is scaled after each timestep, is necessary in these highly non–equilibrium processes in order to emulate heat transfer by phonons.

2.3 Code Development

During my PhD the limitation for large scale MD simulations was shifted. Significant time was invested in code developing. We were able for the first time to simulate high–

energy collision cascades, which required systems that consist of tens to hundreds of millions of atoms, using realistic many–body potentials. The large simulated energies and the increased system size led to implementation and testing of new features in DLPOLY, as well as modification of existing algorithms. That includes on-the-fly analysis of the cascade, improvement of existing algorithms, new feature implementation and, importantly, the implementation of the electronic effects algorithm [54, 55] (see 2.3.6).

2.3.1 Energetic particle

The index, timestep of impact, energy in keV and direction vector of the PKA can be defined using a new radiation damage feature added in the code (*impact i j E x y z* [53]).

2.3.2 Maximum Variable Timestep

By setting a user specified maximum allowed value of the variable timestep, the integration timestep self-adjusts in response to the dynamics of the system and prevents the system from going into an unphysical state (e.g. melting down).

2.3.3 Displaced and Defect atoms

The configurations of our systems have sizes up to tens of GB, making it impossible to save the trajectories of all the atoms in the system for a number of time intervals during the simulation. For this, a new output file is written; the *RSDDAT* file. The *RSDDAT* file contains the atoms of the system that have moved from their initial position more than a cut–off distance d, at user-specified time intervals during the simulation. It accounts for the total number of atoms that have been displaced and describes the elastic deformation of the material. However, some of these atoms recombine to unoccupied crystalline positions and cannot be considered as defects. To account for this effect, the *DEFECTS* file is written in user specified time-intervals, containing only the atoms

that are considered as interstitials or vacancies in the system. We identify the defects using the sphere criterion ([42]): Interstitials are the atoms that are closer than a cut–off distance d to any initial crystalline position (as defined by the initial configuration of the atoms) that has another atom in its vicinity. Accordingly, vacancies are counted as the original atomic sites which have no atom in their vicinity within a radius d [53]. We use $d = 0.75$ Å. d should generally be smaller than half of the closest interatomic separation, and is usually chosen not to account for typical thermal fluctuations of 0.2–0.3 Å. With a certain choice of d, the number of displacements and defect atoms can be compared and agree with other methods of defect identification such as Wigner-Seitz analysis [42].

By writing these files, we quantify the number of induced displacements at each time step and the damage induced in the system during the cascade evolution.

2.3.4 Interatomic potential interpolation

Radiation damage processes are highly non–equilibrium processes, where the PKA transfers large amounts of energy to the particles of the system, resulting in very-short ranged, shorter than 1 Å, interactions. In such highly non–equilibrium conditions the density becomes very inhomogeneous. This resulted in the density to exceed the limits of the embedding function defined for the iron system. The embedding function is a function of the density and it is defined for a specific range of it, which had to be redefined in order to include variations at very short range, where the atoms approach each other in distances shorter than 1 Å. For this a modification in the interatomic potential interpolation was necessary.

2.3.5 Parallel reading and writing issues

Due to the large size of the files (up to hundreds of GB) we encountered issues with the parallel reading of input files and parallel writing of output files. Two new commands were added (*io read*, *io write* [53]) which control how the reading and writing of large files

are performed and how the disk is accessed. These commands improve the performance of the code in regard to handling large files.

2.3.6 Electronic effects

Structural damage induced by ions carrying energies lower than 100 keV is mainly due to ballistic processes [56]. On the other hand, at high–energy events, most of the damage is believed to be due to electronic effects [57]. MD simulations have been used to describe radiation damage effects induced when an energetic particle interacts with the matter creating a collision cascade [58–61]. When fast moving atoms interact with the matter, they lose part of their energy due to their interaction with the electrons. The importance of this interaction in the dynamics of a cascade was first mentioned by Flynn and Averback [62] and the challenge has been to develop models to include the effects of electronic stopping and the electron–ion interactions in MD simulations. These models include proposals by Caro and Victoria [63], Finnis et al.[64], Ivanov and Zhigilei [65] and Duffy and Rutherford [54].

Although electronic stopping has been commonly taken into account in cascade simulations [55, 66–82], there are no systematic studies that include a dynamic, location-dependent description of how the electron-phonon coupling affects the atom dynamics in collision cascades. Examining this issue is especially important in high–energy cascades, where the electronic excitations matter most. In such events, the high–energy ions lose a significant amount of their energy due to the inelastic electronic scattering [54] and high electronic temperatures are expected.

To include these effects we implemented the Two-Temperature model (2T-MD) as described by Rutherford and Duffy [54, 55] in DLPOLY. The implementation was made in two steps: First we implemented the electronic stopping mechanism by including a friction term γ_s in the equation of motion, which applies to atoms with velocities larger than a cut–off value. This way the ballictically moving atoms slow down and the

vibrating atoms do not get affected by the mechanism. Second, we implemented the electron-phonon interaction in terms of an inhomogeneous Langevin thermostat. The full model is described below.

2.3.6.1 Two–temperature Model

The Duffy and Rutherford 2T-MD model [54, 55] has been implemented by our team (Daresbury Laboratory, University College London, Queen Mary, University of London) in DLPOLY code [83, 84] version 4.04, with the support of the *Engineering and Physical Sciences Research Council* (EPSRC). It represents the heat exchange between the ionic and electronic subsystems. Both systems are divided in coarse–grained cells. The effect of inelastic scattering by the electrons is introduced via a friction term in the equation of motion. The equation of motion has the form of a Langevin equation:

$$m\frac{\partial \mathbf{v}_i}{\partial t} = \mathbf{F}_i(t) - \gamma_i \mathbf{v}_i + \widetilde{\mathbf{F}}(t) \tag{2.1}$$

where m is the mass of atom i and $\mathbf{v}_i$ is its velocity. $\mathbf{F}_i(t)$ is the force due to the surrounding atoms of i at time t, γ_i is the friction coefficient and $\widetilde{\mathbf{F}}(t)$ is a random stochastic force term that is determined by the local electronic temperature. The evolution of the electronic temperature is described by the heat diffusion equation given below (see equation 2.6).

The friction term is a sum of two parts: a term that accounts for the effect of electron stopping (γ_s) and is applied for velocities of atoms larger than a cut–off value v_c, and a term that accounts for the electron-ion interaction (γ_p).

$$\gamma_i = \gamma_s + \gamma_p \qquad \text{for} \qquad v_i > v_c \tag{2.2}$$

$$\gamma_i = \gamma_p \qquad \text{for} \qquad v_i \leq v_c \tag{2.3}$$

The cut–off velocity v_c corresponds to energy E_c, which in metals is often taken as approximately double the system's cohesion energy [85] in order to differentiate ballistically moving atoms (with energy in excess of cohesion energy) from those oscillating. In insulators, it has been shown that the band gap governs the electronic energy losses during the radiation damage process [86, 87], and we have accordingly set E_c at twice the band gap.

The magnitude of the stochastic force $\widetilde{\mathbf{F}}(t)$ is related to the friction coefficient by the fluctuation-dissipation theorem and the energy exchange drives the atomic system to the temperature of the electronic subsystem [54]. We assume that atoms gain energy only from the e-p interactions and not from electronic stopping and the stochastic force is proportional only to the e-p interaction friction coefficient γ_p.

$$\langle \widetilde{\mathbf{F}}(t) \rangle = 0 \tag{2.4}$$

$$\langle \widetilde{\mathbf{F}}(t') \rangle . \langle \widetilde{\mathbf{F}}(t) \rangle = 2 k_B T_e \gamma_p \delta(t' - t). \tag{2.5}$$

The MD simulation is coupled to a continuum model for the electronic temperature, which evolves using a heat diffusion equation:

$$C_e \frac{\partial T_e}{\partial t} = \nabla(\kappa_e \nabla T_e) - g_p(T_e - T_\alpha) + g_s T'_\alpha, \tag{2.6}$$

where the second and third terms on the right-hand side of the equation represent energy exchange with the lattice via e-p interactions and electronic stopping, respectively. The second term represents energy exchange with the atomic system energy due to

the difference between the atomic system temperature T_α and the electronic system temperature T_e. The third term is a source term that describes the energy lost by the atomic system due to electronic stopping. C_e and κ_e are electronic specific heat capacity and thermal conductivity, respectively. The atomic temperature T_α is calculated from the average kinetic energy of the atoms in a coarse–grained cell. T'_α has also dimensions of temperature and it is calculated from the average kinetic energy of the subset of atoms with energy greater than twice the cohesive energy of the system [88]. g_p and g_s are the e-p and electronic stopping coupling constants respectively.

The energy loss ΔU_i of an atom i with velocity v_i at each timestep with value Δt due to a friction force F_i is

$$\Delta U_i = \mathbf{F}_i \mathbf{v}_i \Delta t = \gamma_i v_i^2 \Delta t \tag{2.7}$$

In a coarse-grained cell J with constant electronic temperature, the total energy loss will be

$$\Delta U_l = \Delta t \sum_{i \in J} \gamma_{\mathrm{i}} v_i^2 = \Delta t \sum_{i \in J} \gamma_{\mathrm{p}} v_i^2 + \Delta t \sum_{i' \in J} \gamma_{\mathrm{s}} v_i'^2 \tag{2.8}$$

where the second sum is over the atoms that have velocities larger than the cut–off velocity that corresponds to double the cohesive energy of the system. The energy gain of the electronic system at each timestep is

$$\Delta U_{eg} = g_{\mathrm{p}} T_\alpha \Delta V \Delta t + g_{\mathrm{s}} T'_\alpha \Delta V \Delta t. \tag{2.9}$$

Equating ΔU_l and ΔU_{eg} gives

$$\sum_{i \in J} \gamma_{\mathrm{p}} v_i^2 = g_{\mathrm{p}} T_\alpha \Delta V \tag{2.10}$$

$$\sum_{i' \in J} \gamma_{\mathrm{s}} v_i'^2 = g_{\mathrm{s}} T'_\alpha \Delta V \tag{2.11}$$

so T_α and T'_α are defined as

$$\frac{3}{2} k_B T_\alpha = \frac{1}{N} \sum_{i \in J} m v_i^2 \tag{2.12}$$

$$\frac{3}{2} k_B T'_\alpha = \frac{1}{N'} \sum_{i' \in J} m v_i'^2 \tag{2.13}$$

and the coupling constants g_{sp} and g_{s} as

$$g_{\mathrm{p}} = \frac{3 N k_B \gamma_p}{\Delta V m} \tag{2.14}$$

$$g_{\mathrm{s}} = \frac{3 N' k_B \gamma_s}{\Delta V m} \tag{2.15}$$

where N is the number of atoms in a coarse-grained cell J with volume ΔV, k_{B} the Boltzmann constant and N' the number of atoms with velocities larger than v_c in the cell J.

As described in [54], the electronic stopping power is proportional to the ion velocity,

$$\frac{\mathrm{d}E}{\mathrm{d}x} = \lambda E^{1/2} \tag{2.16}$$

$$m \frac{\mathrm{d}u}{dt} = \lambda \left(\frac{m}{2} \right)^{1/2} u \tag{2.17}$$

and the constant of proportionality λ is determined from the Lindhard and Scharff model [89]. Equation 2.17, from eq. 2.1 gives:

$$\gamma_{\mathrm{s}} = \lambda \left(\frac{m}{2}\right)^{1/2} u \tag{2.18}$$

and the corresponding relaxation time for electronic stopping is

$$\tau_{\mathrm{s}} = \frac{m}{\gamma_{\mathrm{s}}} = \frac{(2m)^{1/2}}{\lambda} \tag{2.19}$$

The timescale for energy loss due to e-p interactions is

$$\tau_{\mathrm{p}} = \frac{m}{\gamma_{\mathrm{p}}} \tag{2.20}$$

or from Eq. 2.14

$$\tau_{\mathrm{p}} = \frac{3nk_B}{g_{\mathrm{p}}} \tag{2.21}$$

with n being the number of atoms per unit volume.

The model assumes that the electron-phonon (e-p) coupling process (g_p) is not initiated until thermalisation of the system is achieved. This approximate value was computed by looking at the convergence of kinetic and potential energies in the friction or no–friction cascades. The $C_e(T_e)$ parameterisation for the simulations in α-Fe and W was obtained through *ab initio* calculations [90] and the temperature dependence of electronic thermal conductivity was assumed to be $\kappa_e(T_e) \sim \frac{C_e(T_e)}{C_e(T)}$. We further assume no ionic temperature dependence in $\kappa_e(T_e)$ and a constant value of g_p [90], due to the large uncertainty.

The heat diffusion equation is solved using a finite difference (FD) method. Energy lost by the atoms, due to the friction term, is input into the local FD cell at each MD

timestep. The e-p coupling is modelled by a source/sink term in the heat diffusion equation that depends on the difference between the local electronic and lattice temperatures and the e-p coupling constant. An equivalent amount of energy is removed/added locally to the MD cell by a Langevin thermostat via $\widetilde{\mathbf{F}}(t)$ that depends on T_e.

Additionally, during our simulations with the full two-temperature model switched on, we encountered non anticipated issues related to the computational efficiency of the model, which were related to the different magnitude of the electronic specific heat capacity in different materials. Consequently this difference meant that larger computational effort was needed for the solution of the heat diffusion equation in tungsten than in iron, leading to reduced computational efficiency for the simulation overall. For this, we tested the value for an empirical factor used to determine the number of times the thermal diffusion equation is solved per MD time step, setting it to an optimal value needed for the stable numerical solution/integration of that equation. This achieved stability in the solution of the heat diffusion equation per MD time step and sufficient computational efficiency of the code in order to obtain our results.

2.3.7 Implementation of new boundary scaling thermostat

As mentioned above, in section 2.2.5, the boundaries of the MD simulation box are coupled to a thermal bath. The two available types of temperature scaling algorithms in DLPOLY are (a) the *direct*, which scales the energy of the atoms in the boundary layer to 1.5 $k_{\mathrm{B}}T$ and (b) the *Langevin*, which allows a natural heat exchange between the atoms of the MD box and the atoms of the boundary layer by connecting each atom of the layer to a stochastic heat bath [53].

During our simulations we encountered an interference of the boundary thermostat and the integration algorithms, resulting in an increased ionic temperature, but with no other effect on other properties or simulation outcomes. This interference was observed for the first time, as it was the first time to push the boundaries of what was possible in

MD simulations until recently, and it is under investigation as the reasons are currently unclear. The observation of this interference led to the development of a new type of temperature scaling algorithm, and additionally, the *direct* boundary thermostat is currently under investigation. The new thermostat (*gaussian*) rescales the velocities of the particles contained in the boundary layer in order to give a Maxwell-Boltzmann distribution corresponding to the required temperature, and it is going to be implemented in the public version of the code.

References

[1] B.J. Alder and T.E. Wainwright, Phase transition for a hardsphere system, J. Chem. Phys. **27**, 1208 (1957).

[2] A. Rahman, Phys. Rev. A **136**, 405 (1964).

[3] F. H. Stillinger and A. Rahman, J. Chem. Phys. **60**, 1545 (1974).

[4] J. A. McCammon, B. R. Gelin, and M. Karplus, Nature (Lond.) **267**, 585 (1977).

[5] R.P. Webb abd D.E. Harrison J. Nucl. Instr. and Meth. **218**, 697 (1983).

[6] R.P. Webb and D.E. Harrison J. Phys. Rev. Lett. **50**, 1478 (1983).

[7] T. Diaz de la Rubia, R.S. Averback, R. Benedek and W.E. King, Phys. Rev. Lett. **59**, (1987).

[8] T. Diaz de la Rubia, M.W. Guinan, Phys. Rev. Lett. **66**, 2766 (1991).

[9] W.J. Phythian, C.A. English, D.H. Yellen, D.J. Bacon, Phil. Mag. A **63**, (1991) 821.

[10] M.J. Sabochick, N.Q. Lam, Phys. Rev. B **43**, 5243 (1991).

[11] D.J. Bacon, A.F. Calder, J.M. Harder, S.J. Wooding, J. Nucl. Mater. **205**, 52 (1993).

[12] H. fang Deng, D.J. Bacon, Phys. Rev. B **48**, 10022 (1993).

[13] H. Zhu, R.S. Averback, M. Nastasi, Phil. Mag. A **71**, 735 (1995).

[14] S. M. Woodley and C. R. A. Catlow, Proc. R. Soc. A **467**, 18801884 (2011).

[15] C. R. A. Catlow, R. Bell, F. Cora, S. A. French, B. Slater and A. Sokol, Annu. Rep. Prog. Chem., Sect. A **101**, 513 (2005).

[16] G. H. Gilmer, T. Diaz de la Rubia, D.M. Stock, and M. Jaraiz, Nucl. Instrum. Methods Phys. Res. B **102**, 247-255 (1995).

[17] G. Sastre, C. R. A. Catlow and A. Corma J. Phys. Chem. B, **103**,51875196 (1999).

[18] P. Keblinski, D. Wolf, S. R. Phillpot H. Gleiter, Phil. Mag. A **79**, 2735-2761 (1999).

[19] A.J Haslam, S.R Phillpot, D Wolf, D Moldovan, and H Gleiter, Materials Science and Engineering A **318**, 293312 (2001).

[20] A. H. Fuchs, G. S. Pawley, J. de Physique **49**, 41-51 (1988).

[21] T. Morishita Phys. Rev. Lett. **87**, 105701 (2001).

[22] P. K. Schelling, S. R. Phillpot, D. Wolf, J. Am. Ceram. Soc. **84**, 1609-1619 (2001).

[23] M. W. Finnis, J. E. Sinclair, Philos. Mag. A **50**, 45 (1984).

[24] M. I. Mendelev, S. Han, D. J. Srolovitz, G. J. Ackland, D. Y. Sun, and M. Asta, Phil. Mag. **83**, 3977 (2003).

[25] G. J. Ackland, D. J. Bacon, A. F. Calder, and T. Harry, Philos. Mag. Phys. Condens. Matter Struct. Defect Mech. Prop. **75**, 713 (1997).

[26] S. L. Dudarev, P. M. Derlet, J. Phys.Condens. Matter **17**, 7097 (2005).

[27] A. Souidi, C.S. Becquart, C. Domain, D. Terentyev, L. Malerba, A.F. Calder, D.J. Bacon, R.E. Stoller, Yu. N. Osetsky, and M. Hou, J. Nucl. Mater. **355**, 89 (2006).

[28] D. J. Bacon, Yu. N Osetsky, R Stoller, and R.E Voskoboinikov, J. Nucl. Mater. **323**, 152 (2003).

[29] D.J. Bacon and T. Diaz de la Rubia, J. Nucl. Mater. **216**, 275 (1994).

[30] L. Malerba, M.C. Marinica, N. Anento, C. Bjrkas, H. Nguyen, C. Domain, F. Djurabekova, P. Olsson, K. Nordlund, A. Serra, D. Terentyev, F. Willaime, and C.S. Becquart, J. Nucl. Mat. **406**, 19 (2010).

[31] M. S. Daw, M.I Baskes, Phys Rev. B **29**, 6443 (1984).

[32] J. Tersoff, Phys. Rev. B **38**, 9902-9905 (1988).

[33] E.S. Ferrari, K.J. Roberts, G.B. Thomson, J.D. Gale, C.A. Catlow, Acta Crystallogr. A **57**, 264 (2001).

[34] T. D. Archer, S. E. A. Birse, M. T. Dove, S. A. T. Redfern, J. D. Gale, R. T. Cygan, Phys. Chem. Minerals **30**, 416424 (2003).

[35] D. K. Fisler, J. D. Gale, R. T. Cygan, Am. Mineral **85**, 217224 (2000).

[36] J. Yu, R. Devanathan and W. J. Weber, J. Mater. Chem **19**, 3923 (2009).

[37] M. I. Mendelev and G. J. Ackland Phil. Mag. Lett. **87**, 349 (2007).

[38] A. F. Calder, D. J. Bacon, A. V. Barashev and Y. N. Osetsky, J. Nucl. Mater. **382**, 91 (2008).

[39] K. Morishita and T. Diaz de la Rubia, J. Nucl. Mater. **271**, 35 (1999).

[40] M. Samaras, P. M. Derlet, H. Van Swygenhoven, and M. Victoria, Phys. Rev. Lett. **88**, 125505 (2002).

[41] C. S. Becquart, A. Souidi, C. Domain, M. Hou, L. Marelba and R. E. Stoller, J. Nucl. Mater. **351**, 39-46 (2006).

[42] K. Nordlund, M. Ghaly, R. S. Averback, M. Caturla, T. Diaz de la Rubia and J. Tarus, Phys. Rev. B **57**, 7556 (1998).

[43] Yu. N. Osetsky and D. J. Bacon, J.Nucl.Mater. **323**, 268-280 (2003).

[44] R. E. Stoller, A. F. Calder, J. Nucl. Mater. **283-287**, 746-752 (2000).

[45] A. M. Stoneham, J. R. Matthews and I. J. Ford, J. Phys.: Condens. Matter **16**, S2597 (2004).

[46] K. Trachenko, J. Phys.: Condens. Matt. **16**, R1491 (2004).

[47] K. Trachenko, M. Pruneda, E. Artacho, and M. T. Dove, Phys. Rev. B **70**, 134112 (2004).

[48] K. Trachenko, M. Pruneda, E. Artacho, and M. T. Dove, Phys. Rev. B **71**, 184104 (2005).

[49] S. X. Wang, L. M. Wang, R. C. Ewing, and R. H. Doremus, J. Non-Cryst. Solids **238**, 198 (1998).

[50] T. Hartmann, L. M.Wang, W. J.Weber, N. Yu, K. E. Sickafus, J. N. Mitchell, C. J.Wetteland, M. A. Nastasi, M. G. Hollander, N. P. Baker, C. R. Evans, J. R. Tesmer, and C. J. Maggiore, Nucl. Instrum. Methods Phys. Res. B **141**, 398 (1998).

[51] F. Li, M. Ishimaru, P. Lu, I. V. Afanasyev-Charkin, and K. E. Sickafus, Nucl. Instrum. Methods Phys. Res. B **166-167**, 314 (2000).

[52] H. J. C. Berendsen, J. P. M. Postma, W. van Gunsteren, A. DiNola, J. R. and Haak, J. Chem. Phys. **81**, 3684 (1984).

[53] I.T. Todorov and W. Smith, *THE DL POLY 4 USER MANUAL*, Version 4.04.2, 2013

[54] D. M. Duffy and A. M. Rutherford, J. Phys.: Condens. Mat. **19**, 016207 (2007).

[55] A. M. Rutherford and D. M. Duffy, J. Phys.: Condens. Mat. **19**, 496201 (2007).

[56] R. S. Averback, T. D. de la Rubia, Solid State Physics (ed. H. Erhenfest and F. Spaepen, Academic Press, New York) **51**, 281 (1998).

[57] D. Kanjijal, Current Science **80**, 1560 (2001).

[58] T. Diaz de la Rubia, Nucl. Instr. Meth. Phys. Res. B **120**, 19 (1996).

[59] M. Victoria, S. Dudarev, J.L. Boutard, E. Diegele, R. Lsser, A. Almazouzi, M.J. Caturla, C.C. Fu, J. Kllne, L. Malerba, K. Nordlund, M. Perlado, M. Rieth, M. Samaras, R. Schaeublin, B.N. Singh, and F. Willaime, Fusion and engineering design **82**, 2413 (2007).

[60] S. L. Dudarev, J-L. Boutard, R. Lasser, M. J. Caturla, P. M. Derlet, M. Fivel, C-C. Fu, M. Y. Lavrentiev, L. Malerba, M. Mrovec, D. Nguyen-Manh, K. Nordlund, M. Perlado, R. Schaublin, H. Van Swygenhoven, D. Terentyev, J. Wallenius, D. Weygand, W. Willaime, J. Nuclear Mater. **386**, 1 (2009).

[61] A. V. Krasheninnikov and K. Nordlund, J. Appl. Phys. (Applied Physics Reviews) **107**, 071301, 2010.

[62] C. P. Flynn and R. S. Averback, Phys. Rev. B **38**, 7118 (1988).

[63] A. Caro and M. Victoria, Phys. Rev. A **40**, 2287 (1989).

[64] M. W. Finnis, P. P. Agnew, and A. J. E. Foreman, Phys. Rev. B **44**, 567 (1991).

[65] D. S. Ivanov and L. V. Zhigilei, Phys. Rev. B **68**, 064114 (2003).

[66] V. G. Kapinos and D. J. Bacon, Phys. Rev. B **50**, 13194 (1994).

[67] V. G. Kapinos and D. J. Bacon, Phys. Rev. B **53**, 8287 (1996).

[68] Y. Zhong, K. Nordlund, M. Ghaly and R. S. Averback Phys. Rev. B **58** 2361 (1998).

[69] F. Gao, D. J. Bacon, P. E. J. Flewitt and T. A. Lewis, Modelling Simul. Mater. Sci. Eng. **6**, 543556 (1998).

[70] A. Duvenbeck, F. Sroubek, Z. Sroubek and A. Wucher, Nucl. Instrum. Methods B **225**, 464 (2004).

[71] A. Duvenbeck, F. Sroubek, Z. Sroubek and A. Wucher, Nucl. Instrum. Methods B

228 325 (2005).

[72] A. E. Ismail, J. A. Greathouse, P. S. Crozier and S. M. Foiles, J. Phys.: Condens. Matter **22**, 225405 (2010).

[73] C. L. Phillips, R. J. Magyar, and P. S. Crozier, J. Chem. Phys. **133**, 144711 (2010).

[74] C. P. Race, D. R. Mason and A. P. Sutton, New J. Phys. **12** 093049 (2010).

[75] C. P. Race, D. R. Mason and A. P. Sutton, J. Nucl. Mat. **425**, 3340 (2012).

[76] K. Nordlund and J. Keinonen and A. Kuronen, Physica Scripta **T54**, 34 (1994).

[77] M. H. Shapiro and T. A. Tombrello, Nucl. Instr. Meth. Phys. Res. B **90**, 473 (1994).

[78] K. Nordlund and L. Wei and Y. Zhong and R. S. Averback, Phys. Rev. B (Rapid Comm.) **57**, 13965, 1998.

[79] L. Sandoval and H. M. Urbassek, Physical Review B **79**, 14 (2009).

[80] C. Björkas and K. Nordlund, Nucl. Instr. Meth. Phys. Res. B **267**, 1830 (2009).

[81] S. T. Nakagawa and H. J. Whitlow Nucl. Instr. Meth. Phys. Res. B **268**, 3287 (2010).

[82] D. M. Duffy, N. Itoh, A. M. Rutherford and A. M. Stoneham, J. Phys.: Condens. Matter **20** 082201 2008

[83] I. T. Todorov, B. Smith, K. Trachenko and M. T. Dove, Capability Computing **6**, 12 (2005).

[84] I. T. Todorov, B. Smith, M. T. Dove and K. Trachenko, J. Mater. Chem. **16**, 1911 (2006).

[85] E. Zhurkin and A. Kolesnikov, Nucl. Instrum. Methods Phys. Res., Sect. B, **202**, 269–277, (2003).

[86] J. M. Pruneda, D. Snchez-Portal, A. Arnau, J. I. Juaristi, and Emilio Artacho, Phys. Rev. Lett. **99**, 235501 (2007).

[87] E. Artacho, J. Phys. Condens. Matter, **19**, 275211 (2007).

[88] D.M. Duffy , S. Khakshouri, A.M. Rutherford, Nucl. Instrum. Methods Phys. Res., Sect. B **267**, 3050 (2009).

[89] J. Lindhard and M. Scharff, Mat.-Fys. Medd. K. Dan. Vidensk. Selsk. **27**, 15 (1953).

[90] Z. Lin, L. V. Zhigilei, and V. Celli, Phys. Rev. B **77**, 075133 (2008).

Chapter 3

The nature of high-energy radiation damage in iron

Understanding and predicting a material's performance in response to high-energy radiation damage, as well as designing future materials to be used in intense radiation environments, requires the knowledge of the structure, morphology and amount of radiation-induced structural changes [1–5]. We report the results of molecular dynamics simulations of high-energy radiation damage in iron in the range 0.2–0.5 MeV. We analyze and quantify the nature of collision cascades both at the global and local scale. We observe three distinct types of damage production and relaxation, including reversible deformation around the cascade due to elastic expansion, irreversible structural damage due to ballistic displacements and smaller reversible deformation due to the shock wave. We find that the structure of high-energy collision cascades becomes increasingly continuous as opposed to showing sub-cascade branching reported previously. At the local length scale, we find large defect clusters and novel small vacancy and interstitial clusters. These features form the basis for physical models aimed at understanding the effects of high energy radiation damage in structural materials and serve as a starting point for longer time-scale modeling, such as accelerated dynamics.

3.1 Introduction

Bcc–iron is a base material for ferritic–martensitic bcc steels that are the main candidate materials for structural and plasma facing components of future fusion reactors [6, 7]. The neutrons released in the process carry energy up to 14 MeV, transferring energy up to 1 MeV to Fe atoms they collide with. In this chapter, we study the radiation damage process due to high-energy Fe knock-on atoms of 0.2–0.5 MeV energy. We focus on high-energy radiation damage in α-iron, the main structural material in fission and future fusion reactors. We analyze and quantify the nature of collision cascades both at the global and local scale. We find that high-energy collision cascades may propagate and relax as increasingly continuous damage structures as opposed to showing sub-cascade branching as assumed previously. At the local length scale, we find large clusters and new defect structures.

3.2 Methods

Using DLPOLY program, a general-purpose package designed for large-scale simulations [8, 9], we have simulated systems with 100-500 millions of atoms, and run MD simulations on 20,000–65,000 parallel processors of the HECToR National Supercomputing Service [10]. Equilibration of the system was performed in the NPT ensemble at 300 K. MD simulations were performed at a constant volume, except for the boundary layer atoms that are coupled to a constant temperature thermostat, with the initial temperature set to 300 K. Periodic boundary conditions were imposed in all directions.

We have implemented several features to handle radiation damage simulations. First, we used a variable time step to account for faster atomic motion at the beginning of the cascade development and its gradual slowing down at later stages. Second, the MD box boundary layer of thickness of about 10 Å was connected to a constant temperature thermostat at 300 K to emulate the effect of energy dissipation into the sample. Third,

we have accounted for the electronic energy losses (EEL), particularly important at high energies. EEL is a complicated process that involves a wide range of effects affecting damage production and annealing [2, 11–13].

We model electronic energy loss as a friction term added to the equations of motion. The characteristic energy loss relaxation time (taken here as $\tau_{es} = 1.0$ ps), is obtained by relating the stopping strength ($\lambda = 0.1093$ eV $^{1/2}$Å^{-1})[14] in the low-velocity regime via Lindhard's model to the rate of energy loss for a single atom [15, 16]. Such electronic stopping would only be effective above a certain threshold, where the atoms would have sufficient energy to scatter inelastically. We use a cut-off kinetic energy value (8.6 eV) corresponding to double the cohesive energy of the system [17], however a number of other threshold values have been proposed [18–21]. An atom with velocity corresponding to twice the cohesive energy will travel distance equivalent to the range of the interatomic potential in the time needed for the neighbouring atoms to respond to the impulse of the moving atom (about 0.1 ps) [22].

For α-Fe, we have used a many-body potential [23] that implements the embedded-atom method (EAM) [24]. In this approach each atom is treated as an impurity embedded in a defined electron density [25]. This way the energy of the system is represented as a sum of two terms: the first term is the sum of the pairwise interatomic interactions between the atoms and the second term is a sum of functions representing the electron density:

$$E = \sum_{i=1}^{N-1} \sum_{j=i+1}^{N} V(r_{ij}) + \sum_{i=1}^{N} F(\rho_{ij}) \tag{3.1}$$

$$\rho_i = \sum_{j} f(r_i) \tag{3.2}$$

where i and j represent different atoms, N is the total number of atoms, r_{ij} is distance between atoms i and j and ρ is the electron density.

The many-body EAM potential we used ("M07" from Ref. [26]) is optimized for better reproduction of several important properties of α-Fe including the energetics of point defects and their clusters. The pairwise potential was joined to short-range repulsive ZBL potentials [14] at distances shorter than 1 Å using an exponential polynomial function. The ZBL potential formula is given below (3.3:

$$V_{ZBL} = \frac{Z_1 Z_2}{r_{ij}} \varphi_{r_{ij}} \tag{3.3}$$

where Z_1, Z_2 are the atomic numbers of the elements and $\varphi_{r_{ij}}$ is the screening function

$$\varphi_{r_{ij}} = \sum A_i \exp\left(\frac{-b_i r}{a_{ij}}\right) \tag{3.4}$$

with $a_{ij} = 0.8854\ a_{Bohr}/(Z_1^{0.23} + Z_2^{0.23})$ and the parameters A_i and b_i can be found in [14]. The joining was calibrated against the threshold displacement energies [26]. The resulting thresholds were found to be in as good agreement with experiments as the best previous potentials [26, 27].

To analyze the collision cascade, we have employed two methods. First, an atom is identified as "displaced" if it moves more than distance d from its initial position. The number of displaced atoms, N_{disp}, quantifies the overall amount of introduced damage. Some of this damage recovers back to crystal. To account for this effect, we employed the second method in which an atom is identified as a "defect". An atom is considered an "interstitial" if it is closer to any of the crystalline positions (provided by the initial crystalline reference frame) than distance d and if there is already an atom that is closer to that crystalline site than d. A "vacancy" is defined as a crystalline position (again provided by the initial crystalline reference frame) for which no atom exists close to it within a sphere of radius d. We calculate the number of defect atoms N_{def} as the sum of interstitials and vacancies. Then, N_{def} quantifies both damage production and its recovery. We note that N_{disp} and N_{def} depend on d (we use $d = 0.75$ Å as a convenient

measure). However, the trends discussed in Sec. 3.3, including the two regimes of cascade relaxation as well as dynamics of defects recovery are not sensitive to d provided it is in the sensible range of distances (e.g., too small $d \lesssim 0.1 - 0.2$ Å will be affected by usual thermal fluctuations whereas $d \gtrsim 1 - 1.5$ Å may not identify defect atoms). With a certain choice of d, N_{disp} and N_{def} can be compared and agree with other methods of defect identification such as Wigner-Seitz analysis [28].

Vacancies or self-interstitial atoms (SIA) are defined to belong to the same defect group (cluster) if within 2 nearest-neighbour distance (plus a 20% perturbation). Second nearest-neighbour (nn) is a common clustering criterion for SIAs [29, 30], however the criteria for vacancy clusters vary significantly (from 1 to 4nn) across the literature [31]. When identifying cluster size in the Sec. 3.3 the net defect number (the difference between the number of SIAs and the number of vacancies) is reported.

3.3 Results and discussion

3.3.1 Large-scale damage

We discuss the main features of high-energy collision cascades. To account for potentially different collision cascades due to different knock-on directions, we have simulated 4 different directions for each energy, avoiding low-density directions and associated channeling.

N_{disp} and N_{def} are shown in Fig. 3.1 for 0.2 and 0.5 MeV cascades simulated in different knock-on directions. We observe three distinct types of damage relaxation.

The first type is related to the large peak of $N_{\mathrm{disp}} \approx 10^6$ at short times of about 1–2 ps. This peak relaxes in time τ_{disp} of about about 10 ps. This peak is often discussed as the "thermal spike" [32–34], a phenomenological picture that explores the similarity between the atomic motions in the collision cascade and local melting. In this picture, a collision

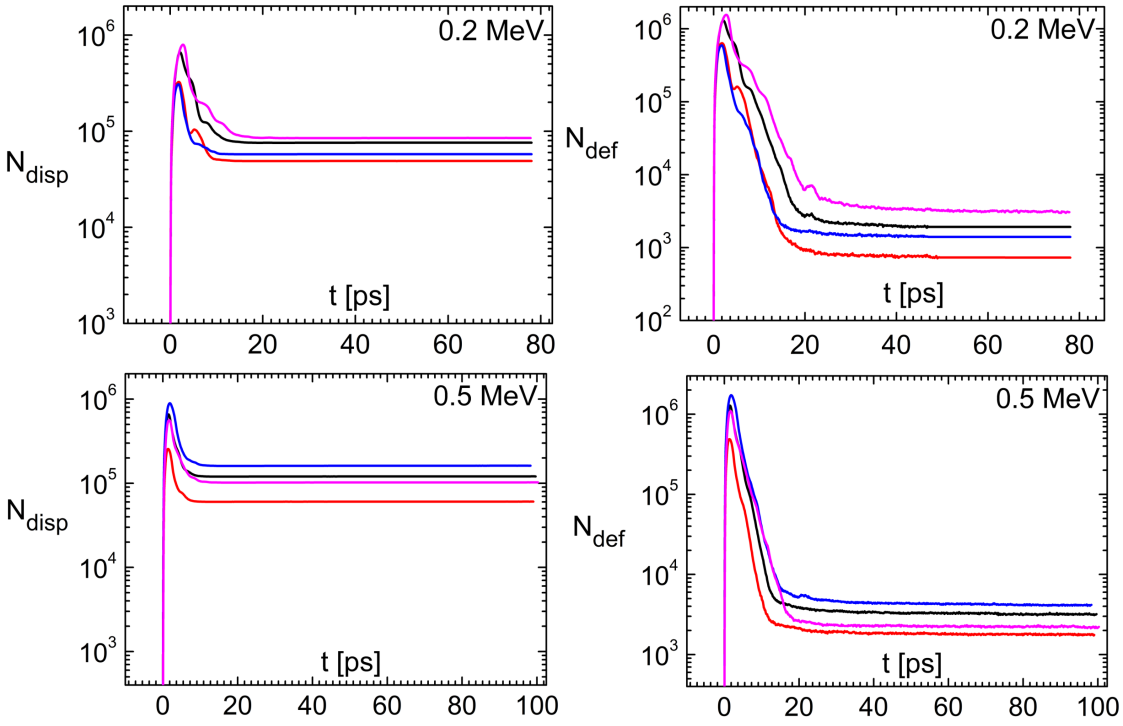

Figure 3.1: N_{disp} and N_{def} from 0.2 MeV (top) and 0.5 MeV (bottom) knock-on atoms for four cascades.

cascade has reduced density because melts have smaller density compared to their solid phases. We note here that the density of some melts (e.g. Si, H_2O and others) around the melting point is actually larger than the density of their parent solid compounds, hence this explanation can not be generally used. In addition, the atomic motions and local density fluctuations in the melt and in the collision cascade are qualitatively different.

We propose that at the atomistic level, the increase of N_{disp} can be understood on the basis of anharmonicity of interatomic interactions: large-scale atomic motion inside the cascade causes the increase of interatomic separations due to anharmonicity. This results in the outward pressure from the cascade on the surrounding lattice and lattice expansion. This elastic deformation lasts several ps, equal to several periods of atomic vibrations during which the energy is dissipated to the lattice, and gives rise to the peak of N_{disp}. Notably, the elastic deformation is reversible irrespective of whether it is followed by the recovery of the structural damage discussed below. In Fig. 3.1, N_{disp}, averaged over all knock-on directions at the end of simulation (corresponding to the flat

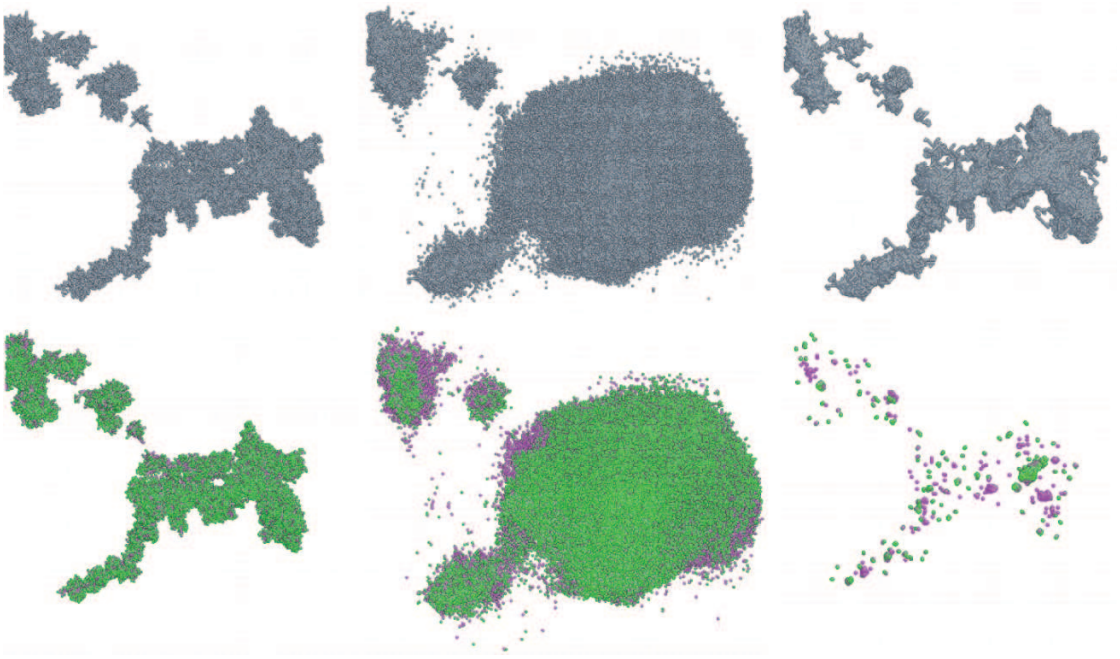

Figure 3.2: Displaced (top) and defect (bottom) atoms in a representative 0.2 MeV collision cascade. The knock-on atom moves from the top left to the bottom right corner. The three frames for each type of atoms correspond to 0.3 ps, 3 ps and 80 ps, respectively. Cascade size (maximal separation between any two atoms in the cascade) is 560 Å. Vacancies (interstitials) are represented in purple (green); we used Atomeye software [35] to visualize cascade evolution.

lines in Fig. 3.1) is about 67,000 and 111,000 atoms for 0.2 MeV and 0.5 MeV cascades, respectively.

Figures 3.2, 3.3 and 3.4 show the snapshots of the collisions cascades at three different stages of cascade development that include the intermediate stage corresponding to the large peak of N_{disp} in Fig. 3.1. Consistent with Fig. 3.1, we observe a significantly larger number of atoms involved in large displacements at intermediate times as compared to the final relaxed state.

The second type of cascade relaxation is related to the dynamics of N_{def}. At short ps times, the large peak of N_{def} is of the same origin as that seen for N_{disp}. However, dynamics of N_{def} also reflect the recovery of structural damage due to ballistic displacements. This recovery proceeds by the diffusion and recombination processes during which atoms

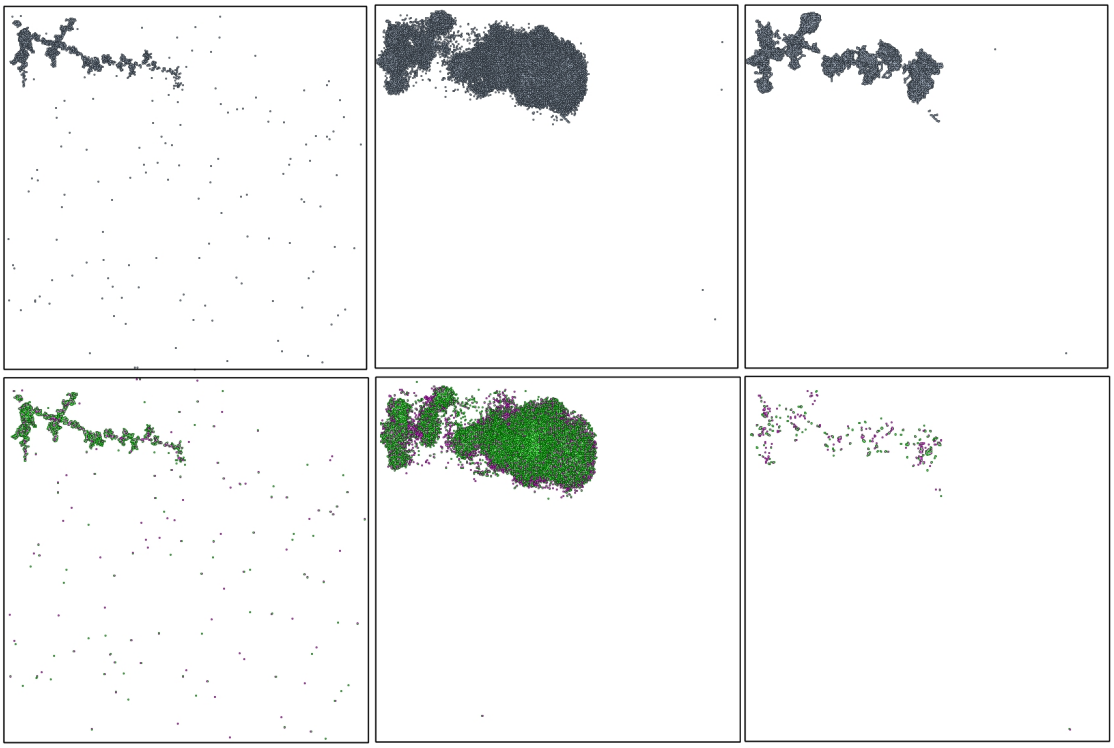

Figure 3.3: Displaced (top) and defect (bottom) atoms in a representative 0.2 MeV collision cascade. The knock-on atom moves from the top left to the bottom right corner. The three frames for each type of atoms correspond to 0.1 ps, 1.8 ps and 50 ps, respectively. Cascade size (maximal separation between any two atoms in the cascade) is 560 Å. Vacancies (interstitials) are represented in purple (green); we used Atomeye software [35] to visualize cascade evolution.

settle at the newly found crystalline positions. This process lasts up to $\tau_{\text{def}} = 20$ ps, significantly longer than the relaxation time τ_{disp} of the first elastic relaxation process as ahown in Fig. 3.1, meaning that the damage recovery lasts longer than the elastic structural relaxation. As a result of this relaxation, N_{def}, averaged over all simulated directions at the end of simulation (corresponding to the flat lines in Fig. 3.1), is about 1,800 and 2,800 atoms for 0.2 MeV and 0.5 MeV cascades, respectively, corresponding to approximately 97% recovery rate as compared to N_{disp}. Such a high recovery rate is in interesting resemblance to some of the resistant ceramic materials, but in contrast to others [36, 37]. Corresponding numbers for N_{disp} and N_{def} at the peak of the damage and at the end of the simulation time for both simulated energies are given in Table 3-A.

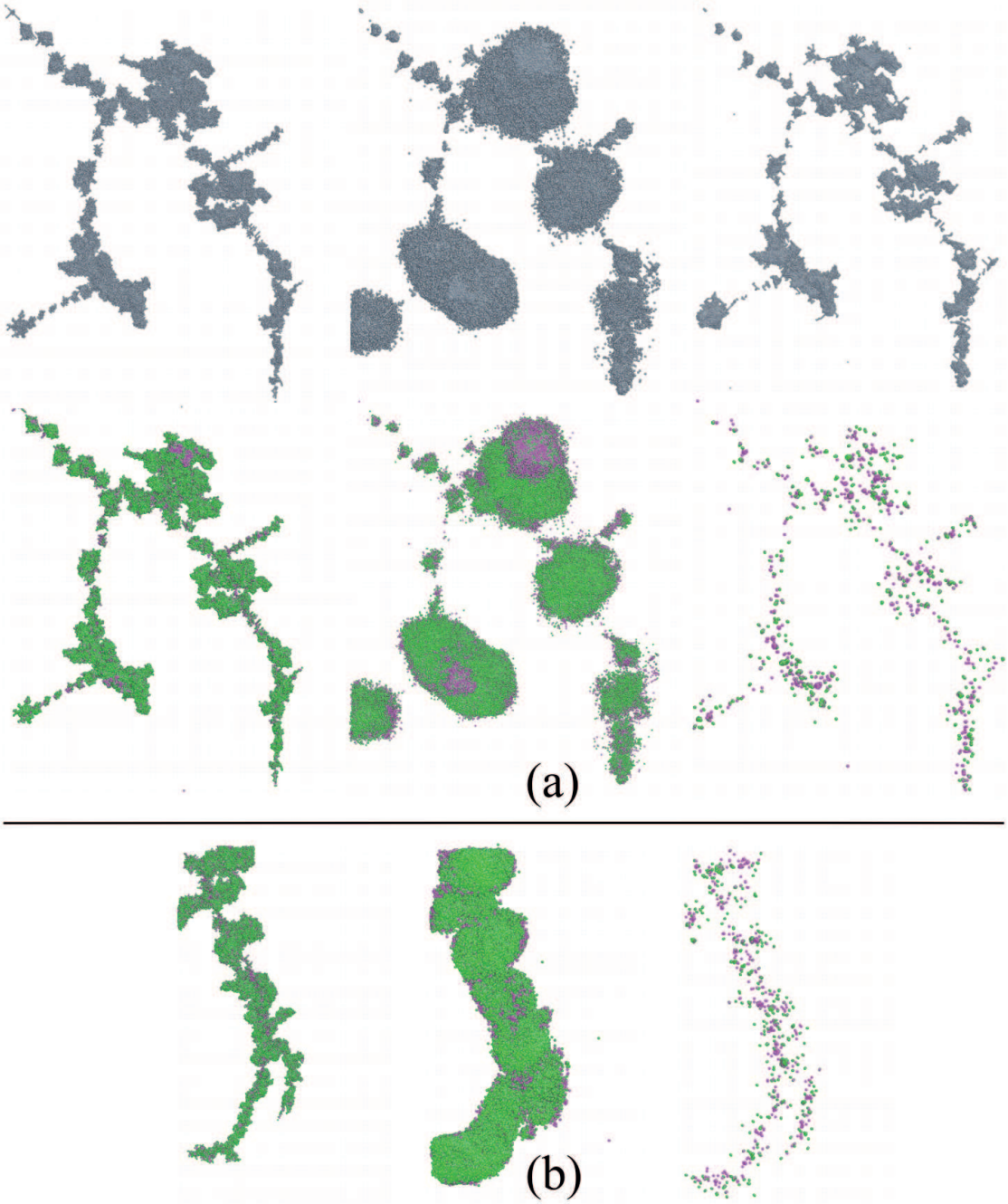

Figure 3.4: (a) and (b) show two representative 0.5 MeV cascades. The knock-on atom moves from the top left to the bottom right corner. In (a) we show both displaced (top) and defect (bottom) atoms at 0.2, 1.5 ps and 100 ps. In (b) we show the defect atoms only at 0.3 ps, 2 ps and 100 ps. Cascade size in (a) and (b) is 950 Å and 1300 Å, respectively.

	PEAK		END	
PKA energy	N_{disp}	N_{def}	N_{disp}	N_{def}
200 keV	523,000 (122,000)	1,020,000 (241,000)	67,000 (8,000)	1,800 (500)
500 keV	593,000 (132,000)	1,147,000 (256,000)	110,000 (21,000)	2,800 (500)

Table 3-A: N_{disp} and N_{def}, calculated using the sphere criterion [28], at the peak of the damage (1-2 ps) and at the end of the simulation. Standard error of the mean is shown in the brackets calculated over four events.

We also find that N_{disp} and N_{def} reported in Fig. (3.1) include displaced and defect atoms that are located throughout the simulation box and away from the moving recoils as seen in the first top and bottom frame of Fig. (3.3). This damage appears in the structure during very short times of 0.1–0.2 ps (before the peak of the damage shown in Fig. (3.1)) and in locations where fast recoils have not yet reached, and can therefore not be due to direct ballistic hits. Consequently, we attribute this damage to the shock wave induced by fast recoils. Indeed, the initial velocity of 500 keV primary recoil atom is about 1314 km/s, or approximately 260 times faster than the speed of sound in iron. Interestingly, we observe displacements induced by the shock wave using the fairly large cutoff displacements distance ($d = 0.75$ Å as discussed above). For 500 keV recoils, N_{disp} and N_{def} due to the shock wave peak are approximately 120 each, i.e. involve much smaller numbers than those involved in two previous types of damage relaxation. After about 0.2 ps, both defect and displaced atoms induced by the shock wave disappear and relax back to crystalline positions. Similar to elastic deformation around the cascade, the deformation due to the shock wave is reversible, although operates on a much shorter time scale.

Our simulations provide an important insight about the structure and morphology of high-energy cascades. The existing view of collision cascades is that they branch out to smaller sub-cascades and "pockets" of damage that are well separated from each other [29]. This takes place over a certain energy threshold, even though this threshold was not firmly established [29, 38, 39]. This picture originated as a result of using binary-collision simulations in combination with MD simulations of low-energy events. Although

involving approximations inherent in binary-collision simulations and extrapolations of low-energy MD simulations, this picture would offer a great degree of reduction and simplification: in analyzing the results and consequences of high-energy damage, only small sub-cascades need to be considered.

In Figures 3.2–3.4, we observe a qualitatively different picture. Cascades branching is visibly reduced as compared to low-energy events, in that we do not find well-separated sub-cascades. Some cascade branching is seen in the first 0.5 MeV cascade shown in Fig. 3.4 (a) only and, importantly, during an intermediate stage of cascade development. On the other hand, the final cascade morphology is described by a rather continuous distribution of the damage across about 1000-1300 Å where no distinctly separated sub-cascades can be identified. Common to all collision cascades we have simulated, this picture is particularly visible for defect atoms in the final state of the cascades shown in Figs. 3.2–3.4.

Qualitatively, reduced cascade branching and the emergence of a more continuous damage distribution can be understood as follows. For a scattered atom to move far enough from its initial position and form a spatially separated sub-cascade (i.e., branch out) requires a large value of energy transferred to it by the incident atom. In the absence of inelastic losses, the transferred energy, T, is $T = \frac{1}{2}T_m(1 - \cos(\phi))$, where T_m is the maximal transferred energy and ϕ is the scattering angle [40]. For large energy of the incident atom, E, ϕ decreases as $\phi \propto \frac{1}{E}$ [40]. We therefore find that for large E and small ϕ, T decreases as $T \propto \phi^2 \propto \frac{1}{E^2}$. Large E and, consequently, small T, results in scattered atoms forming the damaged region close to the trajectory of the initial knock-on atom and, therefore, promotes a continuous structure of the resulting damage. This is consistent with our current findings.

Interestingly, an increasingly continuous structure of cascade morphology observed here is consistent with that seen in irradiation experiments using swift heavy ions [41]. This suggests that the energies simulated in this work broadly correspond to the crossover between the branched and continuous cascade morphology.

We note that as the incident atom slows down, T increases, leading to sub-cascade branching at the end of the atom trajectory. However, larger E results in the increase of the relative fraction of continuous damage over the fraction of branched cascades.

Our finding is important in the context of the long-term evolution of radiation damage. Indeed, a recent kinetic Monte Carlo study [30] has shown that very large defect clusters can have a major effect on the long-term damage development. Hence, our cascade outputs could be used as a starting point for longer time simulations [42]. The final configurations of our systems could be used as input in other simulation methods in order to study the long-term evolution of the defects and their configurations, how they interact with gases and how they can affect the material's performance in long time scales.

3.3.2 Local defects and their clusters

In this part we discuss the defect structures at the local level.

Several mechanisms for local defect clustering have been discussed in the literature. Vacancies have been shown to cluster by the recrystallization front around a heat spike pushing them towards the center of the cascade [43, 44]. This mechanism has been shown to be able to (rarely) produce very large clusters [45]. For the interstitials the situation is more complex. The concept of "interstitial loop punching", well known to be active around high-pressure gas bubbles [46], was suggested to produce interstitial clusters also around heat spikes [47]. Later research, however, showed that it can produce stable damage only near surfaces [48, 49]. Other works have shown that interstitial clusters can be produced in the bulk at least by the isolation of atoms in a liquid pocket left behind a recrystallization front [28] and by shock waves associated with hypersonic recoils [50].

The size and structure of the defect clusters created by the cascades in this work were analyzed and the results are summarized in Table 3-B. The simulations confirm that the normalized fraction of Frenkel pairs (FPs) of 0.3–0.4 is roughly constant for cascades

Cascade energy	0.2 MeV	0.5 MeV
Number of Frenkel Pairs	900 (200)	1450 (220)
NRT fraction of defects	0.44 (0.11)	0.29 (0.04)
Number of isolated vacancies	70 (5)	150 (14)
Number of split SIAs	65 (4)	170 (15)
Number of vacancy clusters	17 (1)	36 (7)
Number of SIA clusters	46 (7)	84 (13)
Largest vacancy cluster	54	47
Largest SIA cluster	89	36

Table 3-B: The number of Frenkel pairs (FP), (N_{F}), and defect statistics for 0.2 MeV and 0.5 MeV cascade simulations in α-iron. The value in brackets shows standard error in the mean over 4 constituent runs for each simulation. Largest clusters are determined by net defect count. NRT fraction is the normalized number of FP [51].

over 0.1 MeV [29, 31]. The fraction of surviving interstitials grouped into clusters was found to be 0.58(3) and 0.52(3) for cascade energies of 0.2 and 0.5 MeV, respectively. This is consistent with the results for 50-100 keV cascades [29, 30] hinting at a possibility that the clustering fraction may reach a maximum at $\sim$ 100 keV. A similar trend was observed for vacancy clustering fractions of 0.33(3) and 0.35(1), respectively.

The majority of interstitial clusters were found to be glissile <111> crowdion clusters, and some of those form dislocation loops with Burgers vector of $b = 1/2 < 111 >$. This is in line with the recent theoretical [52] and experimental results [53], which indicate that for temperatures smaller than 600 K, the $b = 1/2 < 111 >$-type loops are stable, whereas $b =< 001 >$ are unstable. The largest defect structure was a composite 89-interstitial cluster, formed from a merger of a set of <111> and <100> crowdions (Fig. 3.5). Owing to its complex morphology, it will be immobile. This interstitial cluster is quite large, yet consistent with the data reported for lower energies [30, 54].

Large vacancy clusters were also observed with the 54-vacancy cluster being the largest one. Several large vacancy clusters formed <100> and <111> dislocation loop-like configurations [Fig. 3.6(a)]. A cross section of an exemplar vacancy cluster is shown

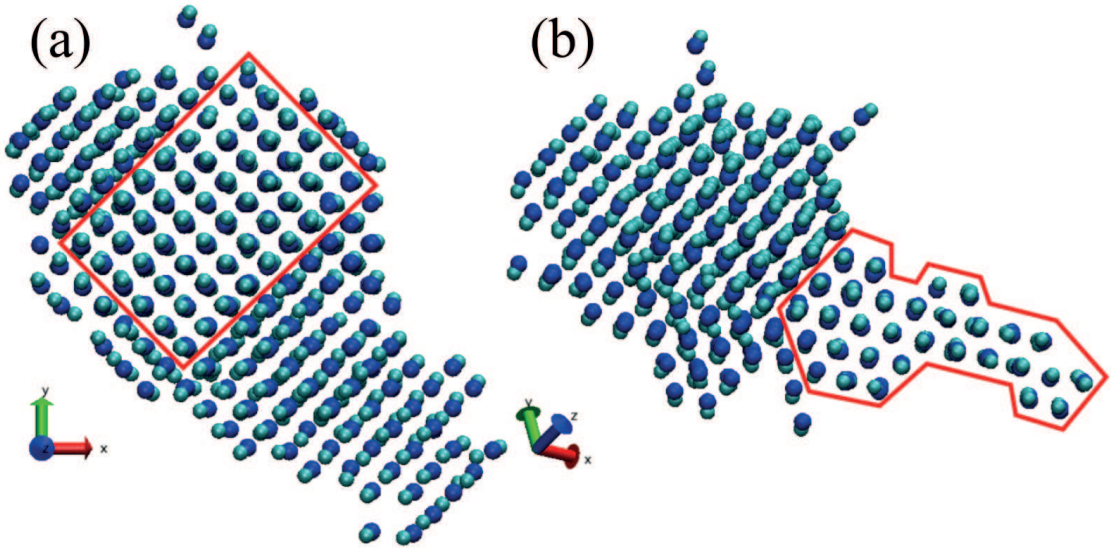

Figure 3.5: The largest cluster consisting of 89 intersitials. It is mainly composed of a set of <100> crowdions (selected region in (a)) and a fraction of normally glissile <111> crowdions (region highlighted in (b)). Such cluster morphology blocks the motion of crowdions and results in an overall sessile cluster; similar effect of immobilization of a cluster by another defect was observed in [55]. Interstitials (vacancies) are shown in silver (blue). We used VMD package for visualization of local defect structures [56].

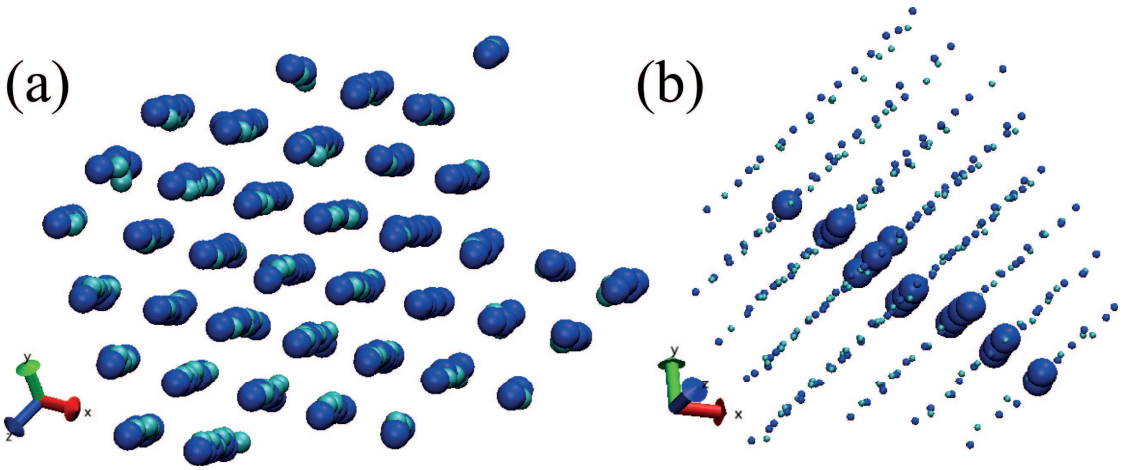

Figure 3.6: (a) A (111) projection of a 39-vacancy cluster; (b) a (001) projection of this cluster. The large spheres show the central vacancy for selected constituent 'vacancy crowdions', thus emphasizing the dislocation nature of the cluster.

[Fig. 3.6(b)], to emphasize its dislocation-like nature. The smaller vacancy clusters revealed a rich variety of structures, such as hexagonal vacancy clusters with interstitial

rings surrounding a central vacancy [Fig. 3.7(a)].

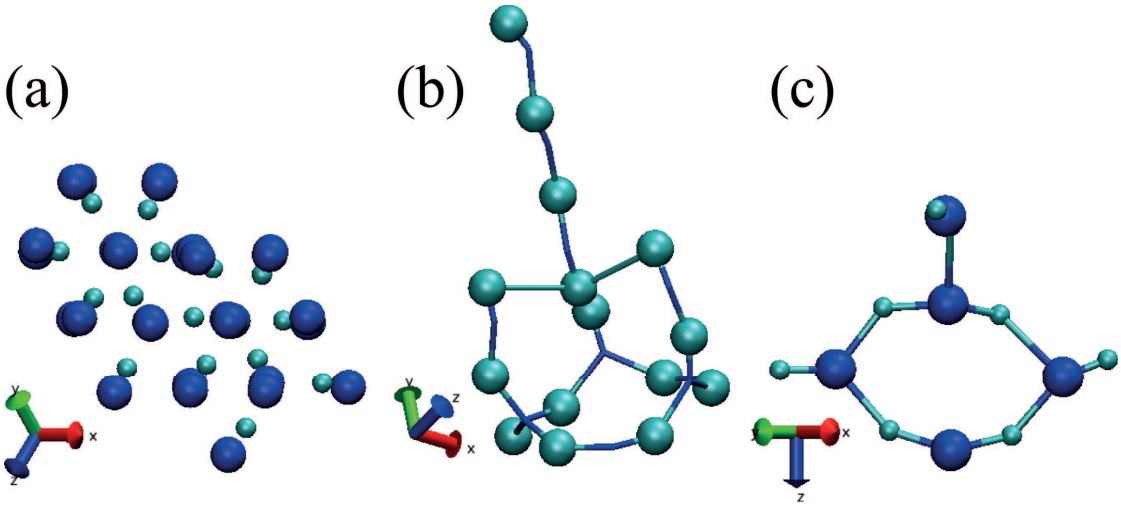

Figure 3.7: (a) The (111) projection of a small 9-vacancy cluster; (b) a C15 phase tetra-interstitial with a <111> crowdion attached. The vacancies are omitted from the figure for clarity; (c) a hexagonal di-interstitial with a split interstitial attached.

We also observed a wide range of sessile interstitial clusters. Some of these could be clearly identified as being related to the C15 meta-stable phase discussed in [57], and many were joined to crowdions or crowdion clusters [Fig. 3.7(b)]. We also observed smaller ring-like structures that have not been observed before [Fig. 3.7(c)] in which 6 atoms shared 4 neighbouring lattice sites.

3.4 Conclusions

In summary, in this chapter novel structural features of radiation damage in iron on both large and local scale have been reported, which will need to be included in physical models aimed at understanding and predicting the effects of radiation damage on the mechanical, thermal and transport properties of structural materials. The reported damage structures such as the increased continuous morphology of high-energy collision cascades will form a starting point for long-timescale models in order to understand and predict the effects of radiation damage. Large defect structures reported here,

including novel vacancy and interstitial clusters, will be important for understanding of the interaction of these clusters with transmutation gases and nucleation of helium bubbles.

References

[1] D. J. Ward and S. L. Dudarev, Materials Today, **11**, 46 (2008).

[2] A. M. Stoneham, J. R. Matthews and I. J. Ford, J. Phys.: Condens. Matter **16**, S2597 (2004).

[3] S. L. Dudarev, J-L. Boutard, R. Lasser, M. J. Caturla, P. M. Derlet, M. Fivel, C-C. Fu, M. Y. Lavrentiev, L. Malerba, M. Mrovec, D. Nguyen-Manh, K. Nordlund, M. Perlado, R. Schaublin, H. Van Swygenhoven, D. Terentyev, J. Wallenius, D. Weygand, W. Willaime, J. Nuclear Mater. **386**, 1 (2009).

[4] W. J. Weber, R. C. Ewing, C. R. A. Catlow, T. Diaz de la Rubia, L. W. Hobbs, C. Kinoshita, Hj. Matzke, A. T. Motta, M. Nastasi, E. K. H. Salje, E. R. Vance and S. J. Zinklea, J. Mater. Res. **13**, 1434 (1998).

[5] A. M. Stoneham and J. H. Harding, Nature Materials **2**, 77, (2003).

[6] D. A. Terentyev, T. P. C. Klaver, P. Olsson, M.-C. Marinica, F. Willaime,4 C. Domain, and L. Malerba1, Phys. Rev. Let. **100**, 145503 (2008).

[7] M. R. Gilbert, S. L. Dudarev, P. M. Derlet and D. G. Pettifor, J. Phys.: Condens. Mat. **20**, 345214 (2008).

[8] I. T. Todorov, B. Smith, K. Trachenko and M. T. Dove, Capability Computing **6**, 12 (2005).

[9] I. T. Todorov, B. Smith, M. T. Dove and K. Trachenko, J. Mater. Chem. **16**, 1911 (2006).

[10] http://www.hector.ac.uk

[11] C. P. Race, D. R. Mason, M. W. Finnis, W. M. C. Foulkes, A. P. Horsfield, and A. P. Sutton, Rep. Prog. Phys. **73**, 116501 (2010).

[12] A. M. Rutherford and D. M. Duffy, J. Phys.: Condens. Mat. **19**, 496201 (2007).

[13] A. Caro, M. Victoria, Phys. Rev. A **40**, 2287 (1989).

[14] J. F. Ziegler, J. P. Biersack, and U. Littmark, The Stopping and Range of Ions in Matter (Pergamon, New York, 1985).

[15] D. M. Duffy, A. M. Rutherford, J. Nucl. Mater., **19**, 386-388 (2009).

[16] J. Lindhard and M. Scharff, Physical Review, **124**, 1, 128130, (1961).

[17] E. Zhurkin and A. Kolesnikov, Nucl. Instrum. Methods Phys. Res., Sect. B, **202**, 269–277, (2003)

[18] M. Jakas and D. Harrison, Phys. Rev. B, **32** 2752–2760, (1985).

[19] K. Nordlund, L. Zhong, and R. Averback. Phys. Rev. B, **57** 965–968, (1998).

[20] J. le Page, D. R. Mason, C. P. Race, and W. M. C. Foulkes, New Journal of Physics, **11**, 1, 013004, (2009)

[21] C. Björkas, K. Nordlund, Nucl. Instrum. Methods Phys. Res., Sect. B, 267 **10**, 1830–1836, (2009)

[22] D. M. Duffy and A. M. Rutherford, J. Phys.: Condens. Mat. **19**, 016207 (2007).

[23] M. I. Mendelev, S. Han, D. J. Srolovitz, G. J. Ackland, D. Y. Sun, and M. Asta, Phil. Mag. **83**, 3977 (2003).

[24] M. S. Daw, M.I Baskes, Phys Rev. B **29**, 6443 (1984).

[25] M. S. Daw, S. M. Foiles, M.I Baskes, Mater. Sci. Reports **9**, 251-310 (1992).

[26] L. Malerba, M.C. Marinica, N. Anento, C. Bjrkas, H. Nguyen, C. Domain, F. Djurabekova, P. Olsson, K. Nordlund, A. Serra, D. Terentyev, F. Willaime, and C.S. Becquart, J. Nucl. Mat. **406**, 19 (2010).

[27] K. Nordlund, J. Wallenius and L. Malerba, Nucl. Instr. Meth. Phys. Res. B **246**, 322 (2005).

[28] K. Nordlund, M. Ghaly, R. S. Averback, M. Caturla, T. Diaz de la Rubia and J. Tarus, Phys. Rev. B **57**, 7556 (1998).

[29] R. E. Stoller, Comprehensive Nuclear Materials **1**, 293 (2012) (Ed. R. J. M. Konings, Elsevier, Amsterdam, 2012).

[30] C. Björkas K. Nordlund and M. J. Caturla, Phys. Rev. B **85**, 024105 (2012).

[31] L. Malerba, J. Nucl. Mat. **351**, 28 (2006).

[32] J. A. Brinkman, J. Appl. Phys. **25**, 961 (1954).

[33] T. Diaz de la Rubia, R. S. Averback, R. Benedeck and W. E. King, Phys. Rev. Lett. **59**, 1930 (1987).

[34] J. Samela and K. Nordlund, Phys. Rev. Lett. **101**, 027601 (2008).

[35] J. Li, Modell. Simul. Mater. Sci. Eng. **11**, 173 (2003).

[36] K. Trachenko, M. T. Dove, and E. Artacho, I. T. Todorov and W. Smith, Phys. Rev. B **73**, 174207 (2006).

[37] K. Trachenko, M. Pruneda, E. Artacho, and M. T. Dove, Phys. Rev. B **71**, 184104 (2005).

[38] K. Nordlund, L. Wei, Y. Zhong and R. S. Averback, Phys. Rev. B **57** 13965 (1998).

[39] H. L. Heinisch, B. N. Singh and T. Diaz de la Rubia, J. Nucl. Mat. **212–215**, 127 (1994).

[40] R. Smith, Atomic and ion collisions in solids and at surfaces (Cambridge University Press, 1997).

[41] K. Trachenko, J. Phys.: Condens. Matt. **16**, R1491 (2004).

[42] X.M. Bai, A.F. Voter, R.G. Hoagland, M. Nastasi, and B.P. Uberuaga, Science **327**, 16311634, (2010).

[43] K. Nordlund and R. S. Averback, Phys. Rev. B **59**, 20 (1999).

[44] K. Nordlund and R. S. Averback, J. Nucl. Mater. **276**, 276 (194).

[45] C. Bjrkas, K. Nordlund and M. J. Caturla, Phys. Rev. B **85**, 024105 (2012).

[46] H. Trinkaus and W. G. Wolfer, J. Nucl. Mater., **122 & 123**, 552 (1984).

[47] T. Diaz de la Rubia and M. W. Guinan, Phys. Rev. Lett. **66**, 2766 (1991).

[48] T. Diaz de la Rubia, Nucl. Instr. Meth. Phys. Res. B **120**, 19 (1996).

[49] K. Nordlund, J. Keinonen, M. Ghaly and R. S. Averback, Nature **398**, 49 (1999).

[50] A. F. Calder, D. J. Bacon, A. V. Barashev and Yu. N. Osetsky, Phil. Mag. **90**, 863 (2010).

[51] M. J. Norgett, M.T. Robinson, I.M. Torrens, Nucl. Eng. Des. **33**, 50 (1975).

[52] S. Dudarev el al, Phys. Rev. Lett. **100**, 135503 (2008).

[53] Z. Yao, M.L. Jenkins, M. Hernndez-Mayoral, and M.A. Kirk, Phil. Mag. **90**, 4623 (2010).

[54] N. Soneda, S. Ishino and T. Diaz de la Rubia, Phil. Mag. Lett. **81**, 649 (2001).

[55] F. Gao, D. J. Bacon, Y. N. Osetsky, P. E. J. Flewitt, and T. A. Lewis, J. Nucl. Mater. **213-220**, 276 (2000).

[56] W. Humphrey, A. Dalke and K. Schulten, J. Molecular Graphics **14**, 33 (1996).

[57] M.-C. Marinica, F. Willaime, and J.-P. Crocombette, Phys. Rev. Lett. **2**, 108 (2012).

Chapter 4

Electronic effects in high-energy radiation damage in iron

Electronic effects are believed to be important in high–energy radiation damage processes where high electronic temperature is expected, yet their effects are not currently understood. In this chapter we discuss the results of molecular dynamics simulations of high-energy collision cascades in α-iron using the coupled two-temperature molecular dynamics (2T-MD) model that incorporates both effects of electronic stopping and electron-ion interaction. We subsequently compare it with the model employing the electronic stopping only, and find several interesting novel insights. The 2T-MD results in both decreased damage production in the thermal spike and faster relaxation of the damage at short times. Notably, the 2T-MD model gives a similar amount of the final damage at longer times, which we interpret to be the result of the combination of smaller amount of short-time damage and shorter time available for damage recovery.

4.1 Introduction

In this chapter we study these effects in high–energy cascades in bcc-Fe, where we include the electron-phonon interaction, in addition to the friction term due to the electronic stopping as described in Chapter 3. We compare cascades where only the electronic stopping mechanism has been included in the simulations with cascades where both the electronic stopping and the electron–ion interactions as well as the energy feed-back from the electronic to atomic system are included. We are referring to the first set of simulations as "friction cascades" and to the second set of cascades that implement the full 2T-MD model as "2T-MD cascades". We see decreased damage production in the thermal spike and faster relaxation of the damage at short times for the 2T-MD cascades. At longer times the 2T-MD model gives a similar amount of final damage, which we interpret to be the combination of two competing effects: smaller amount of short-time damage and shorter time available for damage recovery.

4.2 Methods

In this set of simulations, the exchange of the energy between the atomic and the electronic systems is included, in addition to the previously implemented electronic stopping energy loss mechanism. The model that accounts for both the electronic stopping and the electron-phonon interaction,the 2T-MD model, as introduced by Duffy and Rutherford in [1, 2] is described in Chapter 2.3.3.

The 2T-MD model describes the energy loss of highly energetic atoms due to their interaction with the electrons of the system. According to this model, the energy deposition from the atomic to the electronic system due to the inelastic electronic scattering and the electron-phonon coupling is fed back to the atomic system. The effects of electronic stopping and electron-phonon coupling are included in the simulation of the cascades as a sum of two friction terms in the equation of motion. The redeposition of the energy

to the lattice is described by a stochastic force, which depends on the local electronic temperature. The evolution of the electronic temperature is described by a heat diffusion equation (see below), with the electronic subsystem acting either as a heat sink, removing energy from the atomic system, or a heat bath, returning energy to the atoms [3].

$$C_e \frac{\partial T_e}{\partial t} = \nabla(\kappa_e \nabla T_e) - g_p(T_e - T_\alpha) - g_s T'_\alpha, \tag{4.1}$$

The electronic stopping parameter g_s and the cut-off velocity are as described in Chapter 3. The friction coefficient due to electron-ion interactions corresponds to coupling parameter value of $g_{\mathrm{p}} = 5.4822 \times 10^{18}$ W m $^{-3}$ K^{-1} [4]. The heat capacity C_e given for a range of electron temperatures can be found in [4] and is calculated as described in [5]. A value of $\kappa_{\mathrm{e}} = 80.2$ W m^{-1} K^{-1} for the thermal conductivity at room temperature [6] is used. T_e is the local electronic temperature, T_α is the temperature of the atomic system and T'_α is related to the average kinetic energy of the subset of atoms with energy greater than double the cohesive energy of the system [7].

We are simulating cascades of 100 keV and 200 keV Fe PKAs in bcc–Fe in systems that consist of 30, 50 and 100 million atoms. The NVT ensemble coupled to a Langevin thermostat was applied to all atoms in the system except for the atoms contained in the boundary layer of about 10 Å thickness, where atoms were connected to a constant temperature thermostat. A variable timestep with a maximum value of 1.28×10^{-3} ps is used to describe the atomic motion throughout the cascade development and relaxation. We ran the simulations on up to 65,000 parallel processors of the HECToR National Supercomputing Service [8].

We are using the M07 EAM potential from [9], which is a modification of Mendelev potential for bcc–iron [10], and it is joined to a short-range repulsive ZBL potential [11] for distances shorter than 1 Å, as discussed in the previous chapter.

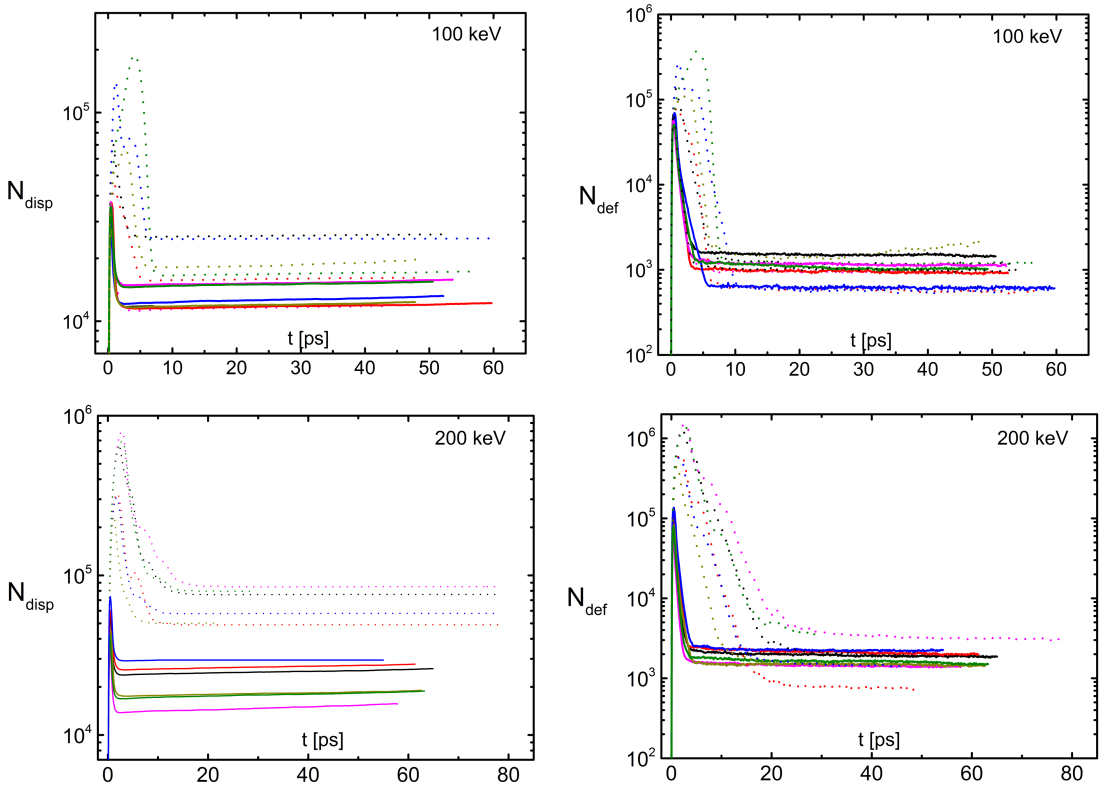

Figure 4.1: N_{disp} and N_{def} (sum of interstitials and vacancies) from 100 keV (top) and 200 keV (bottom) knock-on atoms, for six different PKA directions. Dotted lines represent the friction cascades, while the solid lines are for the 2T-MD cascades.

4.3 Results and Discussion

To describe the damage creation and annihilation we introduce four terms: N_{disp}, N_{def}, τ_{disp} and τ_{def}. As discussed previously, N_{disp} accounts for the total replacements introduced in the system, i.e. is the number of the atoms that have moved more than a cut–off distance from their initial positions. To account for the atoms that recombine to crystalline positions, N_{def} is introduced. N_{def} reflects the recovery of structural damage as it corresponds to the sum of interstitials and vacancies in the system. An atom is considered an interstitial if it is closer to an occupied lattice site than a cut–off distance $d = 0.75$ Å and a vacancy is a crystalline position, for which no atom exists closer to this position than the same distance d [12] (sphere criterion [13]). N_{disp} and N_{def} are shown in fig. 4.1 for 100 and 200 keV cascades simulated in different knock-on direc-

tions. Specifically, with $N^p_{\rm disp}$ we refer to the peak of displaced atoms and with $N^p_{\rm def}$ to the peak of the defect atoms, often referred to as thermal spike [14–16], and $N^l_{\rm disp}$ and $N^l_{\rm def}$ correspond to the number of displaced and defect atoms in long simulation times (the flat lines in fig. 4.1). $\tau_{\rm disp}$ and $\tau_{\rm def}$ are the relaxation times that correspond to the width of $N^p_{\rm disp}$ ($N^p_{\rm disp}$ includes elastic deformation as discussed in Chapter 3) and to the width of $N^p_{\rm def}$ (dynamic annealing) respectively.

Corresponding numbers for $N^p_{\rm disp}$, $N^p_{\rm def}$, $N^l_{\rm disp}$ and $N^l_{\rm def}$ for both simulated energies and for both the friction and the 2T-MD models are given in Table 4-A.

	PEAK		**END**	
PKA energy	$N_{\rm disp}$	$N_{\rm def}$	$N_{\rm disp}$	$N_{\rm def}$
100 keV - friction	89,000 (26,000)	146,000 (47,000)	19,000 (2,000)	1,100 (200)
100 keV - 2T-MD	33,000 (2,000)	61,000 (3,000)	13,000 (700)	1,000 (100)
200 keV - friction	503,000 (98,000)	982,000 (193,000)	66,000 (6,000)	2,000 (400)
200 keV - 2T-MD	52,000 (6,000)	97,000 (11,000)	23,000 (2,000)	1,700 (100)

Table 4-A: $N_{\rm disp}$ and $N_{\rm def}$, calculated using the sphere criterion, at the peak of the damage (1-2 ps) and at the end of the simulation. Standard error of the mean is shown in the brackets calculated over six events.

As seen in Fig.4.1 and Table 4-A, there is a significant difference in $N^p_{\rm disp}$ and $N^p_{\rm def}$ as well as in $\tau_{\rm disp}$ and $\tau_{\rm def}$ for both models and simulated energies. First, both $N^p_{\rm disp}$ and $N^p_{\rm def}$ are smaller for the 2T-MD cascades as compared to the friction cascades. Second, $\tau_{\rm disp}$ and $\tau_{\rm def}$ are shorter for the 2T-MD cascades, corresponding to about 3 ps and 5 ps for $N^p_{\rm disp}$ and $N^p_{\rm def}$ respectively, for both simulated energies. These differences are due to faster quenching of the thermal spike in the 2T-MD model that includes the electron-phonon coupling and the additional energy transfer channel. In effect, the e-p coupling removes energy from the thermal spike and electronic thermal conductivity transports it from the simulation cell. This additional energy loss mechanism in the 2T-MD model is also responsible for the smaller amount of unrecombined damage at long times, $N^l_{\rm disp}$, as is seen in Figure 4.1.

An interesting insight comes from the examination of $N^l_{\rm def}$ which quantifies the final

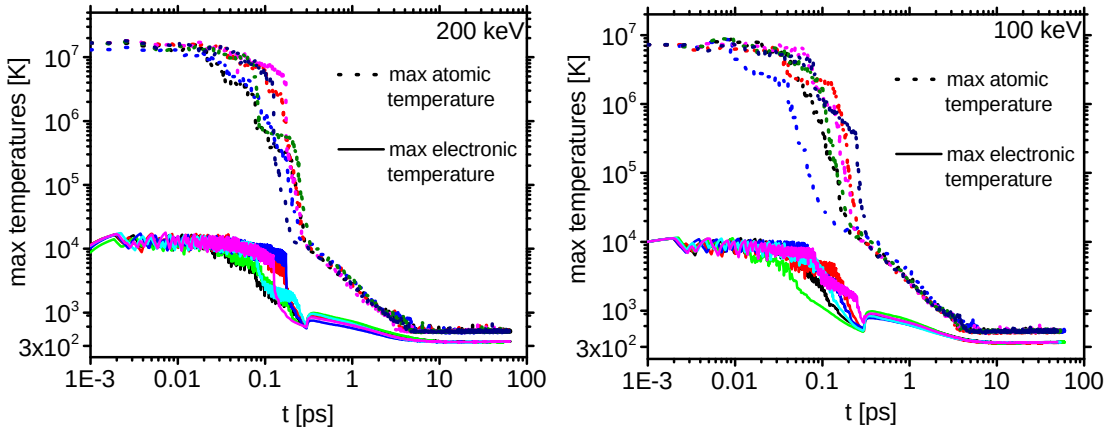

Figure 4.2: Maximum electronic and atomic temperatures for 200 keV (left) and 100 keV (right) 2T-MD cascade simulations, for six events.

amount of damage in the structure and ultimately governs the radiation response of the system. We observe that $N^l_{\rm def}$ is similar in both 2T-MD and friction models (see Figure 4.1 and Table 4-A). This effect can be understood on the basis of two competing mechanisms. On one hand, energy transfer to the electrons reduces the short–time displaced atoms production, $N^p_{\rm disp}$. On the other hand, faster energy transfer also reduces the time of the thermal spike in Figure 4.1, the time that is available for most efficient and fast recombination in the highly mobile and disordered state. As a result, $N^l_{\rm def}$ in the 2T-MD cascades are similar to $N^l_{\rm def}$ in the friction cascade where the initial amount of the damage, $N^p_{\rm def}$ is larger but relaxation time is longer. Figure 4.2 shows the maximum electronic and atomic temperatures for 100 keV and 200 keV 2T-MD cascades, where for all simulations the atomic temperature is higher than the electronic, meaning that the electronic system acts as a heat sink. This is in agreement with lower energy (10 keV) 2T-MD cascades in iron [1].

In Figures 4.3, 4.4 and 4.5, 4.6 we show representative 100 keV and 200 keV cascades for the same PKA direction showing the effects discussed above. Figure 4.3 shows three different time–frames of the relaxation of a representative cascades in a 30 million atoms system, for a 100 keV Fe PKA, where the electronic stopping effect is switched on. The top images illustrate the displaced atoms and the bottom images illustrate the defect

Figure 4.3: A representative 100 keV cascade where the friction mechanism is switched on. The PKA moves from the top left to the bottom right corner. Displaced atoms are shown in the top frames of the figure and defect atoms in the bottom frames. The simulation box length is 700 Å and the systems consists of about 30 million atoms. The cascade size is about 300 Å. The snapshots are at 0.1, 2.5 ps (peak of the damage) and 48 ps. Vacancies (interstitials) are represented in purple (green). We used Atomeye software [17] to visualize cascade evolution.

atoms on the system. Fig. 4.4 shows three snapshots of the displaced (top) and defect (bottom) atoms for a typical 2T-MD cascade for a 100 keV Fe PKA.

The middle frames in figures 4.3 and 4.4 demonstrate the difference in displaced (about 70,000 for friction and 40,000 for 2T-MD cascade) and defect atoms (115,000 for friction and 70,000 for 2T-MD cascade) for the two mechanisms and correspond to the peaks shown in the top plots of Fig.4.1. The peak for the 2T-MD cascade is at shorter time, 0.4 ps, than for the friction cascade, 2.5 ps demonstrating faster relaxation. $N^l_{\rm disp}$ is 20,000 and 15,000 for friction and 2T-MD cascades respectively. $N^l_{\rm def}$ is 2,000 for both the friction and the 2T-MD cascade, which is consistent with Fig.4.1 (flat lines in the

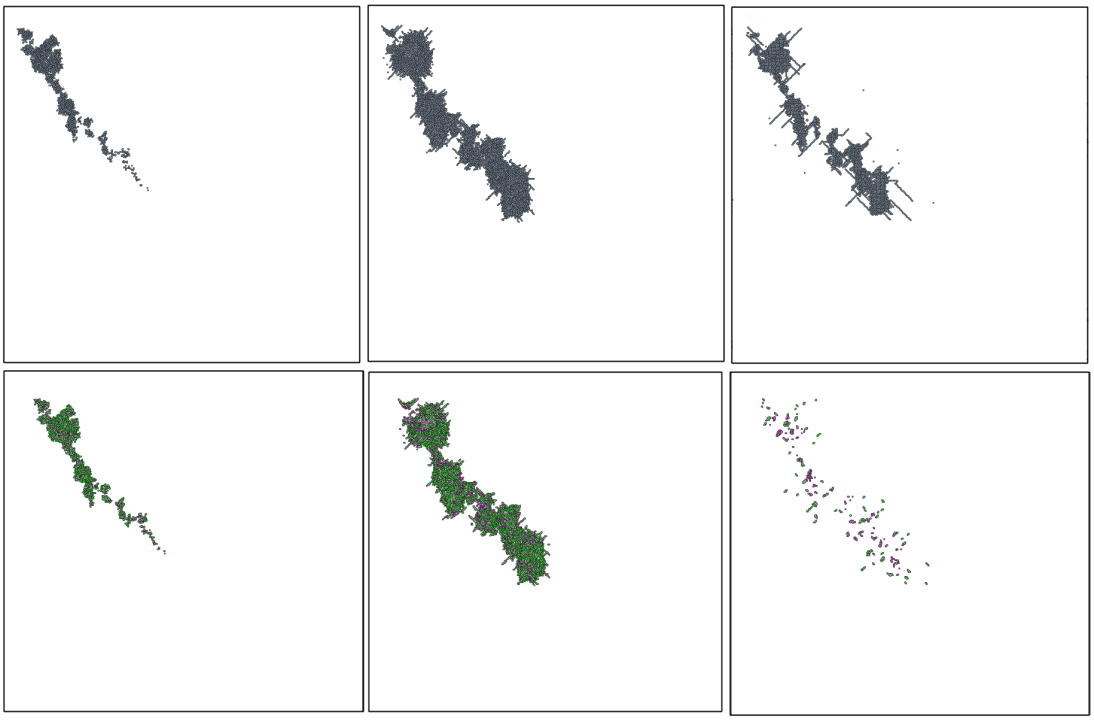

Figure 4.4: A representative 100 keV cascade where the the full 2T-MD is implemented. The PKA moves from the top left to the bottom right corner. Displaced atoms are shown in the top frames of the figure and defect atoms in the bottom frames. The simulation box length is 700 Å and the systems consists of about 30 million atoms. The cascade size is about 500 Å. The snapshots are at 0.1, 0.4 (peak of the damage) and 53 ps. Vacancies (interstitials) are represented in purple (green). We used Atomeye software [17] to visualize cascade evolution.

top plots).

Smaller $N^p_{\rm disp}$, $N^p_{\rm def}$ and $N^l_{\rm disp}$ and shorter $\tau_{\rm disp}$ and $\tau_{\rm def}$ for 2T-MD cascades demonstrated in Fig.4.1 (bottom) are also shown in Fig. 4.5 and 4.6. Fig. 4.5 - 4.6 show the snapshots of two typical 200 keV collision cascades at three different stages of development, for the friction mechanism and the 2T-MD model respectively. Displaced atoms are shown in the top frames and the defect atoms are shown in the bottom frames.

The middle frames of these figures correspond to the peaks shown in Fig.4.1 (bottom). $N^p_{\rm disp}$ is 250,000 and 50,000 for the friction and the 2T-MD cascade. $N^p_{\rm def}$ is 450,000 and 80,000 for the friction and 2T-MD cascade. $N^l_{\rm disp}$ and $N^l_{\rm def}$, corresponding to the flat

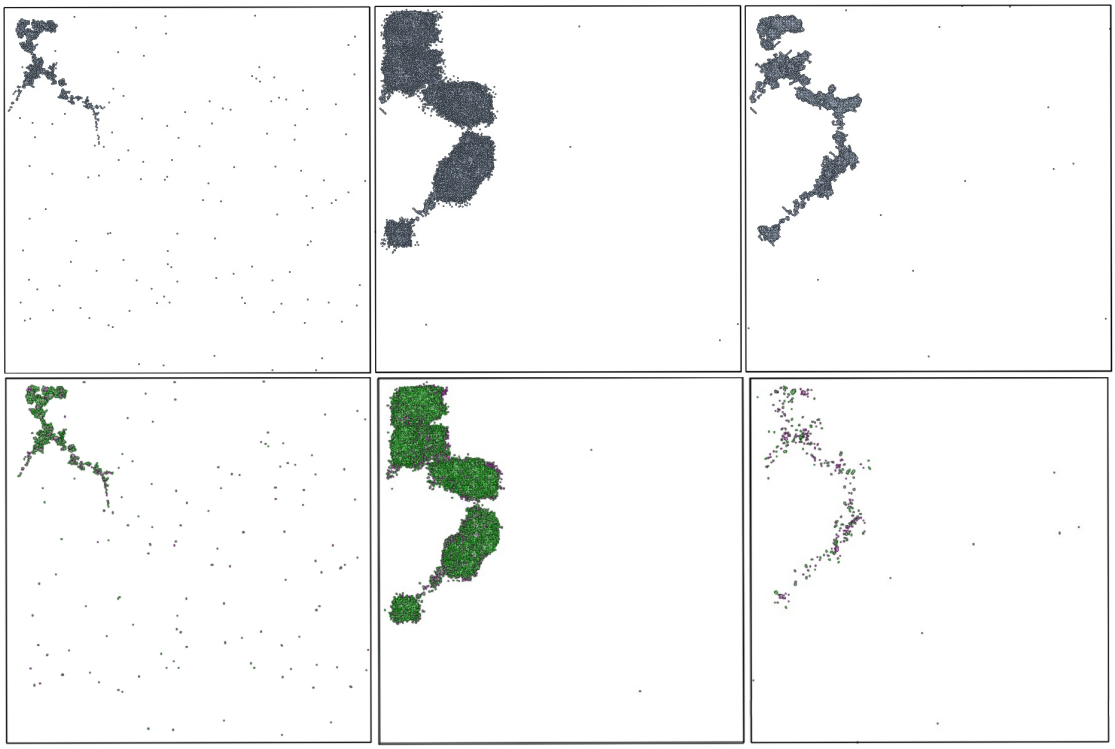

Figure 4.5: A representative 200 keV cascade where the friction mechanism is switched on. The PKA moves from the top left to the bottom right corner. Displaced atoms are shown in the top frames of the figure and defect atoms in the bottom frames. The simulation box length is 1100 Å and the systems consists of about 50 million atoms. The cascade size is about 800 Å. The snapshots are at 0.1, 1.2 ps (peak of the damage) and and 22 ps. Vacancies (interstitials) are represented in purple (green). We used Atomeye software [17] to visualize cascade evolution..

lines at longer times in the bottom plots of Fig.4.1, are shown in the third frames of these figures. N^l_{dsip} is 50,000 and 20,000 for the friction and 2T-MD cascade. N^l_{def} for both mechanisms is 1,500 atoms, in consistency with Fig.4.1. For both 100 keV and 200 keV cascades shown in fig. 4.3–4.6, we can see that the two models result in different shape of the cascade. Faster quenching of the cascade when the 2T-MD model is applied results in different distribution of the energy and this in turn results in different shape and, in some cases, different size of the cascade.

The discussion on the large–scale analysis above focused on the comparison of the dynamics of the two models. Defect analysis results at the local level are summarized in

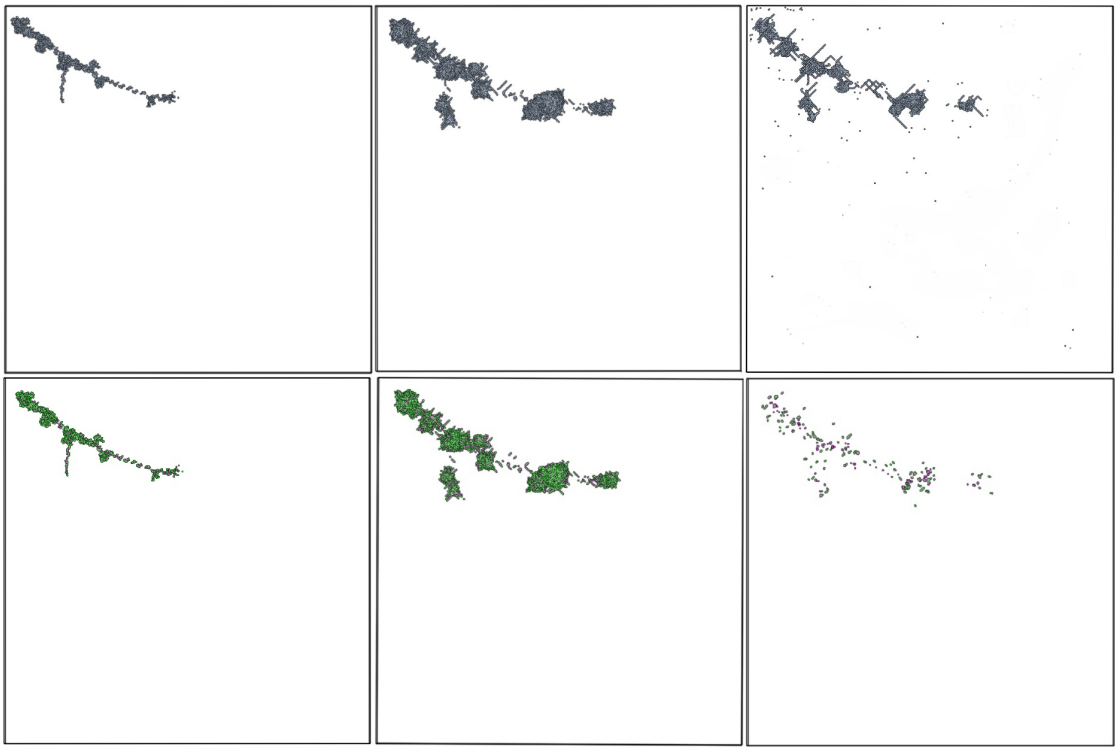

Figure 4.6: A representative 200 keV cascade where the the full 2T-MD is implemented. The PKA moves from the top left to the bottom right corner. Displaced atoms are shown in the top frames of the figure and defect atoms in the bottom frames. The simulation box length is 1100 Å and the systems consists of about 50 million atoms. The cascade size is about 800 Å. The snapshots are at 0.1, 0.5 (peak of the damage) and 63 ps. Vacancies (interstitials) are represented in purple (green). We used Atomeye software [17] to visualize cascade evolution.

Table 4-B, where statistics for the defect clusters for the friction and the 2T-MD cascades are given. As discussed above, the difference in the remaining number of FP between the two models is small. Similar statistics of defect analysis were obtained for the 100 keV friction and 2T-MD cascades. As shown in the table, we observe statistically significant differences in terms of distribution of defects and their clusters for the 200 keV cascades. In particular, the number of isolated vacancies and interstitials is about two times higher for the 2T-MD results than for the friction model. The number of SIA clusters is much smaller for the 2T-MD model at 200 keV. This shows that the differences in 2T-MD model and friction model cascade dynamics (see above) can have significant effects on

PKA energy	**100 keV friction**	**100 keV 2T-MD**	**200 keV friction**	**200 keV 2T-MD**
N_{FP}	550 (200)	500 (100)	1000 (400)	850 (100)
Number of isolated vacancies	15 (2)	16 (2)	19 (2)	32 (3)
Number of isolated SIAs	58 (9)	68 (6)	55 (8)	126 (9)
Number of vacancy clusters	26(4)	38 (5)	75 (6)	64 (5)
Number of SIA clusters	3 (1)	6 (1)	67 (4)	13 (11)
Largest vacancy cluster	18	21	56	12
Largest SIA cluster	11	12	89	8

Table 4-B: The number of Frenkel pairs (N_{FP}),calculated using the sphere criterion, and defect distribution statistics for 100 keV and 200 keV friction and 2T-MD cascade simulations in α-iron. Standard error of the mean is shown in the brackets calculated over six events. The largest clusters that we found in each set of six simulations are presented in the last two columns and are determined by net defect count which is the difference between the number of self–interstitial atoms (SIAs) and the number of vacancies.

damage clustering.

4.4 Conclusions

Previous works on cascades in Fe have shown that the fraction of damage in clusters depends both on the interatomic potential and the way electron-phonon coupling and electronic stopping is included in the cascades [9, 18]. The fraction of damage in large clusters, in turn, may have a major effect on the long-time scale evolution of damage, and is hence a crucial issue for developing predictive radiation-damage modelling [19]. In this work we are using the full two temperature model for the first time in energies where the electronic effects matter most. The results show further that treating the

electron-phonon coupling in a local way significantly affects the fraction of damage in clusters. Taken together, these results show that assessing accurately the reliability of primary radiation damage simulations in metals requires consideration not only of the interatomic potentials, but also a local model for the electron-phonon coupling. Hence, this study opens a new avenue of investigation of electronic effects in other materials, for example in tungsten, which is chosen as a divertor material in fusion reactors [20], and which we discuss in Chapter 5.

References

[1] D. M. Duffy and A. M. Rutherford, J. Phys.: Condens. Mat. **19**, 016207 (2007).

[2] A. M. Rutherford and D. M. Duffy, J. Phys.: Condens. Mat. **19**, 496201 (2007).

[3] A. M. Stoneham, Nucl. Instrum. Methods B **48**, 389 (1989).

[4] http://www.faculty.virginia.edu/CompMat/electron-phonon-coupling

[5] Z. Lin, L. V. Zhigilei, and V. Celli, Phys. Rev. B **77**, 075133 (2008).

[6] Y.G. Li, W.H. Zhou, L.F. Huang, Z. Zeng, and X. Ju, Fusion Eng. Des. **86**, 2812 (2011).

[7] D.M. Duffy , S. Khakshouri, A.M. Rutherford, Nucl. Instrum. Methods Phys. Res., Sect. B **267**, 3050, (2009).

[8] http://www.hector.ac.uk

[9] L. Malerba, M.C. Marinica, N. Anento, C. Bjrkas, H. Nguyen, C. Domain, F. Djurabekova, P. Olsson, K. Nordlund, A. Serra, D. Terentyev, F. Willaime, and C.S. Becquart, J. Nucl. Mat. **406**, 19 (2010).

[10] M. I. Mendelev, S. Han, D. J. Srolovitz, G. J. Ackland, D. Y. Sun, and M. Asta, Phil. Mag. **83**, 3977 (2003).

[11] J. F. Ziegler, J. P. Biersack, and U. Littmark, The Stopping and Range of Ions in Matter (Pergamon, New York, 1985).

[12] K. Trachenko, M. T. Dove, and E. Artacho, Phys. Rev. B **73** 174207 (2006).

[13] K. Nordlund, M. Ghaly, R. S. Averback, M. Caturla, T. Diaz de la Rubia and J. Tarus, Phys. Rev. B **57**, 7556 (1998).

[14] J. A. Brinkman, J. Appl. Phys. **25**, 961 (1954).

[15] T. Diaz de la Rubia, R. S. Averback, R. Benedeck and W. E. King, Phys. Rev. Lett. **59**, 1930 (1987).

[16] J. Samela and K. Nordlund, Phys. Rev. Lett. **101**, 027601 (2008).

[17] J. Li, Modell. Simul. Mater. Sci. Eng., **11**, 173 (2003).

[18] C. Björkas and K. Nordlund, Nucl. Instr. Meth. Phys. Res. B **267**, 1830, (2009).

[19] C. Björkas, K. Nordlund and M. J. Caturla, Phys. Rev. B **85**, 024105, (2012).

[20] R. Neu et al., Phys. Plasmas **20**, 056111 (2013).

Chapter 5

High-energy Radiation Damage in Tungsten

The Joint European Torus (JET) has recently produced tungsten samples irradiated in fusion reaction sustained for several minutes [1]. Hence, research into high energy radiation damage in tungsten is timely and of great importance. We recently initiated this project of investigating high energy induced damage in tungsten, and in this chapter we discuss our first findings. First we discuss the electron–phonon coupling effect in the simulations, finding it to result in less residual damage. Then we study the effect of temperature by comparing high-energy radiation damage in 300 K and 800 K, finding that high temperature promotes damage recovery. This is an ongoing work, with findings to be extended, analyzed and published in the full form soon.

5.1 Introduction

Tungsten and tungsten alloys are candidate materials for the divertor armor in fusion reactors due to their high melting point, high thermal conductivity, reduced deuterium retention and low sputtering erosion [2–5]. Tungsten has been recently used as divertor

armor material in recent fusion experiments [1], where it is subject to intense irradiation. Irradiation of a material results in defect creation. Defects play an important role in the material's performance as they can alter its properties, e.g. thermal conductivity and brittleness. Hence, fundamental research of the interaction of the radiation with matter is important.

The 14 MeV neutrons produced in fusion can transfer energy up to 300 keV to a tungsten atom, which will induce the creation of a collision cascade in the system, resulting in the creation of point defects and their clusters. Previous studies have investigated radiation effects in tungsten due to lower energy PKAs up to some tens of keVs [6–10]. A recent study of Nordlund et al [11] studied collision cascades due to 150 keV PKAs at 0 K, taking into account the electronic stopping mechanism. In this work we shift the limitations of low PKA energy, low temperature irradiation and absence of the electron-phonon coupling and we simulate collision cascades of 300 keV energy PKAs, including in our simulations both the electronic stopping mechanism and the electron–phonon interaction. Particles moving with velocities that correspond to this high energy lose important part of their energy due to their interaction with the electrons, hence it is important to include in the simulations the electronic effects. We simulate high–energy radiation damage effects in tungsten at room temperature and at 800 K, the fusion reactor's operating temperature.

We study two effects: first, we study the electron-phonon coupling effects on the cascade evolution. For this, we simulate cascades with only the electronic stopping mechanism applied and we compare them with cascades for which we have applied the full two–temperature model. We refer to the first set of the cascades as "friction cascades" and to the second as "2T-MD cascades". Second, we investigate the temperature effects on the induced damage in the system, by simulating collision cascades at both 300 K and 800 K.

5.2 Methods

We simulate five randomly chosen directions of the PKA in a system consisting of about 30 million atoms in ambient temperature and at 800 K, the fusion reactor's operating temperature. The NVT ensemble coupled to a langevin thermostat was applied to all atoms in the system except in the boundary layer of about 10 Å thickness, where atoms' velocities are scaled in order to emulate the energy dissipation in the sample. A variable timestep, ranging from 0.01 fs to 3.2 fs, is used to describe the atomic motion throughout the cascade development and relaxation.

The electronic effects are included in the simulations as described in Chapter 2 and Chapter 4. For the performance of the friction cascades only the friction term that corresponds to the electronic stopping is switched on. The electronic stopping friction coefficient was calculated using SRIM tables [12] to a value of 1.1 ps^{-1} and is applied to atoms that move with velocity larger than a value that corresponds to double the cohesive energy of the system. The friction coefficient due to electron-ion interactions corresponds to coupling parameter value of $g_p = 7 \times 10^{17}$ W m $^{-3}$ K^{-1} [13]. The heat capacity given for a range of electron temperatures can be found in [14] and is calculated as described in [15]. A value of $\kappa_e = 174$ W m^{-1} K^{-1} and 125 W m^{-1} K^{-1} for the thermal conductivity at room temperature and at 800 K [16, 17] respectively is used.

We are using a modified embedded-atom potential for tungsten [18] joined to the short range repulsive ZBL potential using a polynomial spline, fitted to reproduce the experimentally obtained defect threshold energies. The same potential has been used by Nordlund et al [11] for the simulation of 150 keV cascades at 0 K. We ran the simulations on up to 32,000 parallel processors of the HECToR National Supercomputing Service.

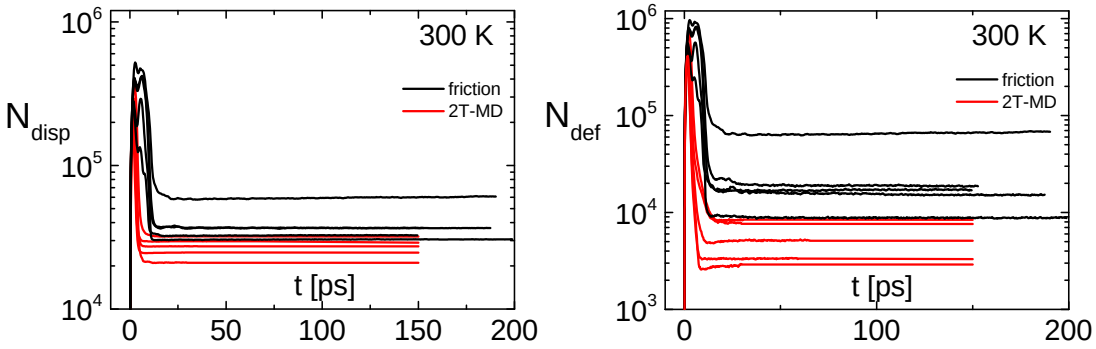

Figure 5.1: Number of displaced (left) and defect (right) atoms for five 300 keV friction cascades (black lines) and five 2T-MD cascades (red lines) at 300 K.

5.3 Results and Discussion

Damage creation and recovery is illustrated in Fig. 5.1. $N_{\rm disp}$ and $N_{\rm def}$ are used, as described earlier, to identify the total number of displacements in the sample and the total number of defects, as the sum of interstitials and vacancies. We use the same cut-off distance $d = 0.75$ Å using the sphere criterion [19] as for the simulations discussed in the previous chapters. $N_{\rm disp}$ and $N_{\rm def}$ can be compared and agree with other methods of defect identification such as Wigner-Seitz analysis [19] with a certain choice of d, which needs to eliminate the thermal fluctuations.

We will use $N^p_{\rm disp}$ to refer to the peak of displaced atoms and with $N^p_{\rm def}$ to the peak of the defect atoms, and $N^l_{\rm disp}$ and $N^l_{\rm def}$ to refer to the number of displaced and defect atoms in long simulation times (the flat lines in Fig. 5.1). $\tau_{\rm disp}$ and $\tau_{\rm def}$ are the relaxation times that correspond to the width of $N^p_{\rm disp}$ (elastic deformation) and to the width of $N^p_{\rm def}$ (dynamic annealing) respectively.

5.3.1 Electron-phonon coupling effect

In Fig. 5.1 we see $N_{\rm disp}$ and $N_{\rm def}$ as a function of time for friction (black lines) and 2T-MD (red lines) cascades performed at 300 K. In agreement with our findings for iron, when the 2T-MD model is applied the relaxation times $\tau_{\rm disp}$ and $\tau_{\rm def}$ are smaller than the relaxation times for the friction cascades. For the friction cascades $\tau_{\rm disp}$ and $\tau_{\rm def}$ are about 10-15 ps, and for the 2T-MD cascades about 5 ps and 10 ps respectively. Interestingly, there is no significant difference in $N^p_{\rm disp}$ and $N^p_{\rm def}$ between the two models, but the 2T-MD model results in significantly less residual damage at the end of the simulation. On average, the fraction of $N_{\rm def}({\rm friction})/N_{\rm def}({\rm 2T-MD})$ at the end of the simulation time is about 5.

The small difference in the produced damage at the peak and the significant difference in the remaining damage in the system are in contrast to our findings for iron, as discussed in Chapter 4. For iron we found that the 2T-MD model results in reduced damage in the thermal spike (the peaks shown in the plots of Fig. 5.1) and in small difference of remaining defects. This difference could be due to different values of parameters in the 2T-MD model as is currently investigated.

In Fig. 5.2 we see the relaxation of a typical 2T-MD cascade at 300 K, in a system consisting of about 30 million atoms. The simulation box has length of about 800 Å and the cascade size is about 450 Å. This figure illustrates continuous morphology of the collision cascade, which is in agreement to our results for higher energy events in iron and zirconia.

The significant difference in the remaining damage demonstrates the need to accurately simulate high-energy collision cascades by including in the simulations a local model to describe the electron–phonon coupling. The diversity of the results of the 2T-MD model in iron and tungsten demonstrate the importance of taking into account the electronic effects in these high energies and emphasizes the need to avoid extrapolations of results obtained for one material to others, even in a case like tungsten, which has

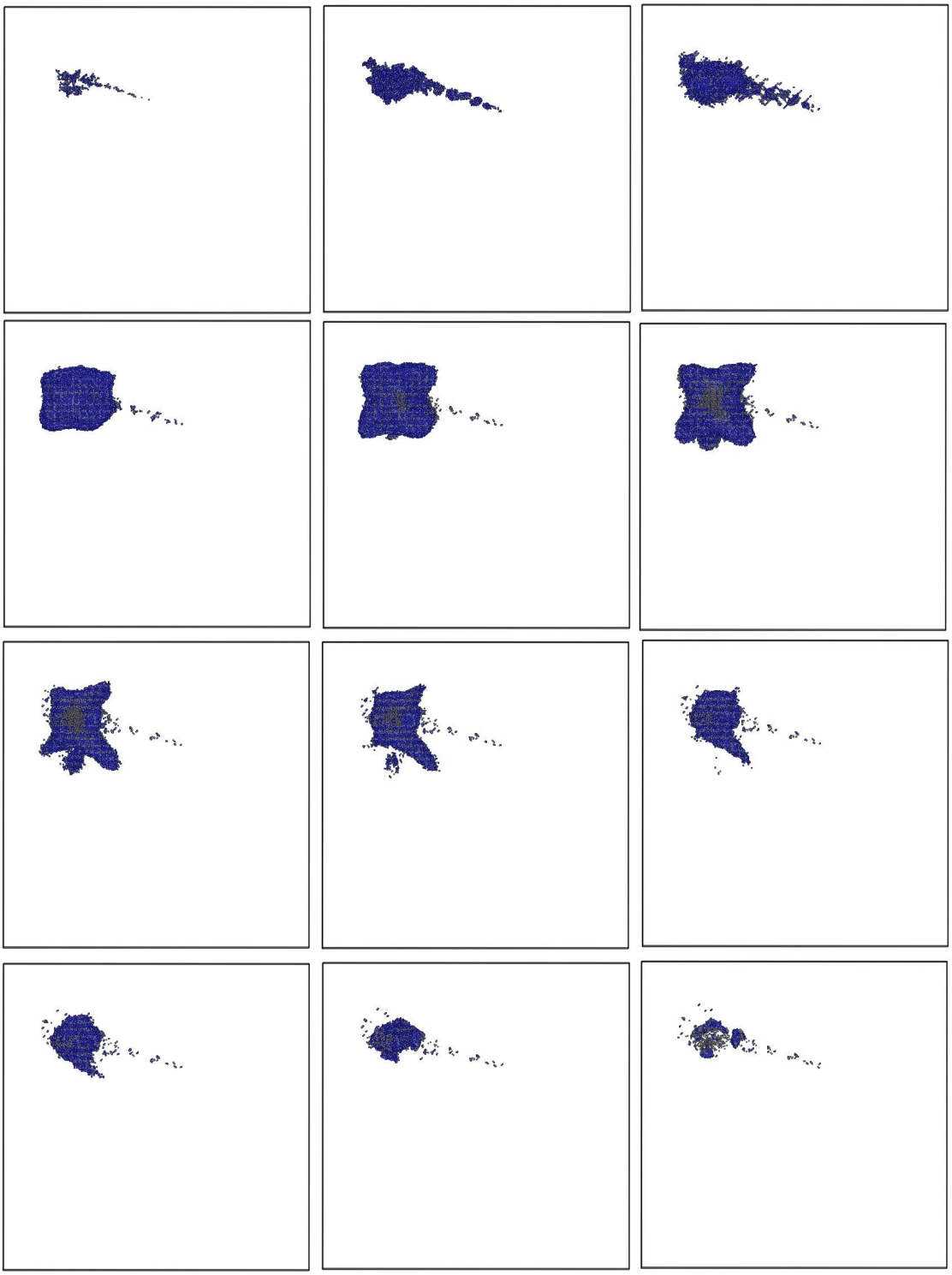

Figure 5.2: Relaxation of a 300 keV 2T-MD cascade performed at 300 K in a system consisting of about 30 million atoms. The simulation box has about 800 Å length. The simulation time is 30 ps. Interstitials are shown in blue and vacancies in grey.

the bcc structure like iron. Our findings show that implementing a model to account for the electron-phonon coupling in high-energy collision cascades can significantly affect the resulting damage in the system quantitatively. Additionally, the electronic effects can significantly affect the fraction of damage in clusters, resulting in different defect structures. This highlights that radiation damage in metals requires not only an accurate interatomic potential, but importantly, the consideration of the e-p coupling in a local way.

5.3.2 Temperature effect

We discuss radiation damage due to 300 keV tungsten PKAs in systems consisting of 30 million atoms at 300 K and 800 K with full account of the electronic effects. Fig 5.3 illustrates N_{disp} and N_{def} for five collision cascades at 300 K (blue line) and at 800 K (green line). Here we observe larger N^{p}_{disp} and N^{p}_{def} for the 800 K collision cascades, meaning that there is larger number of displacements and damage creation in the thermal spike for the cascades performed at higher temperature. As seen in the flat lines at long simulation time, the resulting displacements and resulting damage N^{l}_{disp} and N^{l}_{def} are smaller in 800 K simulations compared to 300 K simulations. This suggests that high temperature promotes damage recovery. The activation barriers for damage recovery are surmounted faster at higher temperature, allowing as to see this process on the timescale of 100 ps in the MD simulation. On average, the fraction of $N_{\mathrm{def}}(300)/N_{\mathrm{def}}(800)$ at the end of the simulation time is about 2.

The outcomes of these simulations will be further analysed and compared with a recent experimental study of irradiation of tungsten with 150 keV recoils at about 800 K, where dislocations and loops are observed [20]. In Fig. 5.4 we present local defect structures, dislocation-like clusters and loops, observed in two typical 2T-MD cascades due to 300 keV recoils at 800 K.

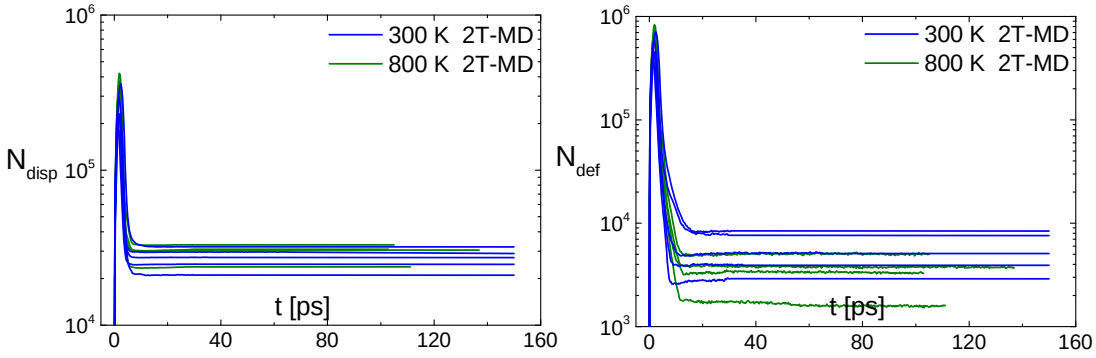

Figure 5.3: Number of displaced (left) and defect (right) atoms for five 300 keV 2T-MD cascades at 300 K (in blue colour) and at 800 K (in green colour).

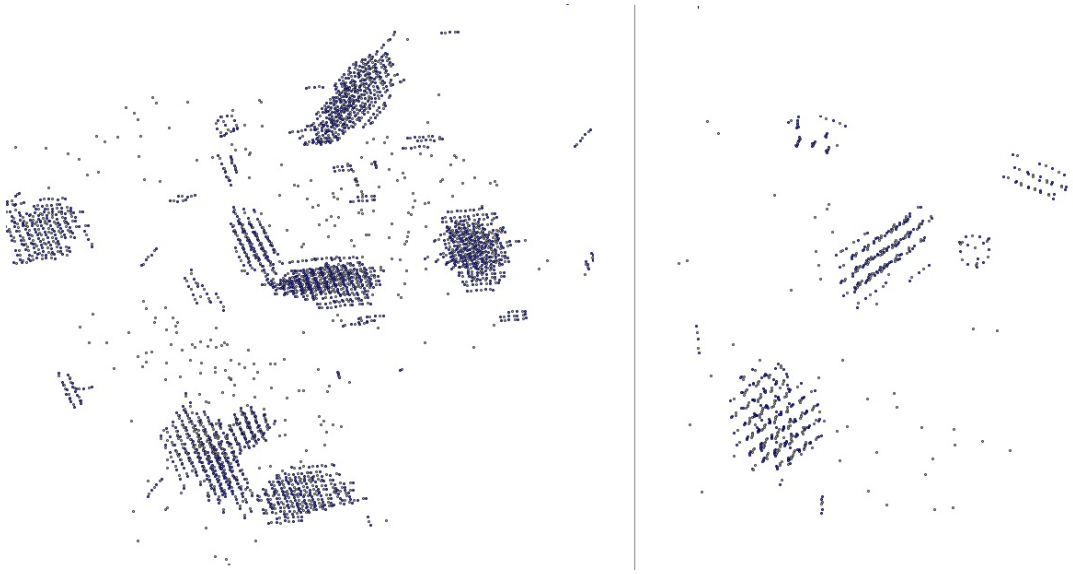

Figure 5.4: Local defect structures (dislocation-like clusters and loops) in two typical 2T-MD 300keV cascades performed at 800 K. Interstitials are shown in blue and vacancies in grey.

5.4 Conclusions

In this Chapter we presented the first results of high energy radiation damage in tungsten in 300 K and 800 K. Our findings showed the importance of taking into account the electronic effects in high energy collision cascade simulations. If we ignore the electronic effects we might overestimate the induced damage in the system. We simulated

high-energy collision cascades at the fusion reactor's operating temperature, finding that higher temperature promotes damage recovery resulting in less residual damage in comparison to cascades performed at 300 K. The work presented in this chapter is in progress and will be finalized with further analysis of the data and be published in the full form soon. The timeliness of this project is significant: indeed, fusion is now possible experimentally, and simulation of the radiation damage effects in materials related to fusion has now become feasible. The combination of both presents us a unique opportunity and a chance to make a substantial step towards fusion of tomorrow.

References

[1] R. Neu et al., Phys. Plasmas **20**, 056111 (2013).

[2] B.Q. Fu at al., J. Nucl. Mater. **427**, 268 (2012).

[3] T. Hirai, G. Pintsuk, J. Linke, and M. Batilliot, J. Nucl. Mater. **390**, 751754 (2009).

[4] M. Li, J. Wang, Q. Hou, J. Nucl. Mater. **423**, 2227 (2012).

[5] M. H. J. t Hoen, M. Mayer, A.W. Kleyn, H. Schut, and P.A. Zeijlmans van Emmichoven, Nucl. Fusion **53**, 043003 (2013).

[6] B. Fu, B. Xu, W. Lai, Y. Yuan, H. Xu, C. Li, Y. Jia, and W. Liu, Jour. Nucl. Mater. **441**, 2428 (2013).

[7] T. Troev, N. Nankov, and T. Yoshiie, Nucl. Instr. Meth. Phys. Res. B **269**, 566-571 (2011).

[8] J. Fikar and R. Schaeublin, Nucl. Instr. Meth. Phys. Res. B **255**, 27-31 (2007).

[9] N-Y. Park, P-R. Cha, Y-C. Kim, H-K Seok, S-H. Han, S-C. Lee, S. Cho, and H. Jung, Met. Mater. Int. **15**, 447-452 (2009).

[10] M. W. Finnis, P. Agnew, and A. J. E. Foreman, Phys. Rev. B, **44**, 567 (1991).

[11] A. E. Sand, S. L. Dudarev, and K. Nordlund, arXiv:1306.3824

[12] http://www.srim.org/

[13] S. Khakshouri and D. M. Duffy, Phys. Rev. B **80**, 035415 (2009).

[14] http://www.faculty.virginia.edu/CompMat/electron-phonon-coupling

[15] Z. Lin, L. V. Zhigilei, and V. Celli, Phys. Rev. B **77**, 075133 (2008).

[16] CRC Handbook of Chemistry and Physics 90th Edition, Ed: David R. Lide, 2010.

[17] Y. G. Li, W. H. Zhou, L.F. Huang, Z. Zeng, and X. Ju, Fusion Eng. Des. **86**, 28122820 (2011).

[18] C. Bjrkas, K. Nordlund, and S. Dudarev Nucl. Instr. Meth. Phys. Res. B **267**, 32043208 (2009) and Erratum Nucl. Instr. Meth. Phys. Res. B **268**, 1529 (2010).

[19] K. Nordlund, M. Ghaly, R. S. Averback, M. Caturla, T. Diaz de la Rubia and J. Tarus, Phys. Rev. B **57**, 7556 (1998).

[20] X. Yi, M.L. Jenkins, M. Briceno, S.G. Roberts, Z. Zhou, and M.A. Kirk, Phil. Mag. **93**, 17151738 (2013).

Chapter 6

Uncovering the hidden damage in irradiated zirconia

Zirconia is viewed as a material of exceptional resistance to amorphization by radiation damage, and consequently proposed as a candidate to immobilize nuclear waste and serve as an inert nuclear fuel matrix. Here, we perform molecular dynamics simulations of radiation damage in zirconia in the range of 0.1-0.5 MeV energies with account of electronic stopping energy losses. Surprisingly, we find that the lack of amorphizability co-exists with a large number of point defects and their clusters. These, importantly, are largely isolated from each other and therefore represent a dilute damage that does not result in the loss of long-range structural coherence and amorphization. We document the nature of these defects in detail, including their sizes, distribution and morphology, and discuss practical implications of using zirconia in intense radiation environments.

6.1 Introduction

Zirconia, ZrO_2 (both in cubic and monoclinic form), stands out on the list of materials that are highly resistant to amorphization: both in-situ and ex-situ experiments

such as X-ray diffraction, Rutherford backscaterring spectroscopy, transmission electron microscopy (TEM) and so on indicated no loss of crystalline structure in bulk samples under bombardment with heavy MeV-energy ions, up to very high doses and at low temperature of about 20 K, and plutonium doping [1–8]. This was considered as evidence for the exceptional resistance to amorphization compared to other materials [9, 10] and, combined with its ability to incorporate radioactive ions from nuclear waste including actinides [11], zirconia has been considered as a strong candidate material for inert fuel and nuclear waste matrices [1–8, 12–17].

An important question arises regarding what the high resistance to amorphization implies for the purposes of using zirconia as a waste form. The experimental probes above provide the information about the long-range order, and in many cases do not directly probe the nature of point defects and clusters smaller than several nanometers. Instead, these probes indirectly study the macroscopic consequences such as lattice swelling. This issue has been recently receiving increasing attention in the context of elucidating the *local*, as opposed to long-range, structure [18]. In the case of zirconia, point defects and small clusters of point defects may not affect the Bragg peaks up to the smallest k-vectors, yet play an important role in defect-assisted diffusion processes involving the radioactive ions. Point defects have been seen in irradiated zirconia, although determination of their exact structure, abundance and distribution has been viewed as challenging [1–8]. In this chapter, we address this question using MD simulations, a method that provides access to detailed structural changes at the atomistic scale. We find that high-energy radiation creates unexpectedly large amount of damage. Importantly, this damage is contained in point defects and small clusters of point defects, and therefore does not constitute what is usually considered as amorphization in terms of the loss of long-range order, an insight that we additionally verify by direct calculation of the radial distribution function. We discuss the implications of our findings for using zirconia as a waste form.

Interaction	A_{ij} [eV]	ρ_{ij} [Å]	C_{ij} [eV Å^6]	Charges [e]
O-O	1388.7730	0.3623	175.0000	O: -1.2
Zr-O	17243.394	0.2265	128.3513	Zr: 2.4
(U-O)				U: 2.4

Table 6-A: Buckingham potential parameters from [21].

6.2 Methods

In this work, we perform MD simulations of radiation damage in cubic zirconia due to high energies in the 0.1–0.5 MeV range. To contain the damage due to these energies, we use system sizes with lengths of up to 130 nm and 150 millions of atoms, using DLPOLY program [19, 20]. We have used the interatomic potential that includes Buckingham pair interaction potentials and partial Coulomb charges [21]. Buckingham potential is given by:

$$U_{ij} = A_{ij} \exp\left(\frac{-r_{ij}}{\rho_{ij}}\right) - \frac{C_{ij}}{r_{ij}^6} \tag{6.1}$$

where r_{ij} is the distance between two sites i and j, and the Buckingham parameters A_{ij}, ρ_{ij} and C_{ij} are given in table 6-A.

The system was equilibrated in the constant pressure ensemble at 300 K. A U atom was chosen as a primary recoil atom to correspond to the alpha-decay process, and was given a range of velocities corresponding to the energy of 0.1–0.5 MeV, and its propagation was followed in the NVE (0.1 MeV no friction cascades) or NVT (friction cascades) ensemble. As discussed in the previous chapters, we have used a variable time step to account for faster atomic motion at the beginning of the cascade development and its gradual slowing down at later stages. A boundary layer of the MD box of about 10 Å thickness was coupled to a Langevin thermostat at 300 K to emulate the effect of energy dissipation into the sample. We have accounted for the electronic energy losses, particularly important at high energies, by implementing the friction-type term

in the equations of motion applied to particles above the certain cutoff energy E_c (or velocity) [22, 23]. As discussed previously, in metals, E_c is often taken as approximately the double of the system's cohesion energy in order to differentiate ballistically moving atoms (with energy in excess of cohesion energy) from those oscillating. In insulators, it has been shown that the band gap governs the electronic energy losses during the radiation damage process [24, 25], and we have accordingly set E_c at twice the band gap in zirconia. The friction coefficient was calculated using the SRIM tables [26]. Finally, the Buckingham potential was joined to a repulsive ZBL potential [27] (see equations 3.3 and 3.4) at short distances using a switching function [28]. The simulations were run on 3200–65000 parallel processors of UK's National Supercomputing Facilities, HECToR.

We have simulated recoils of 0.1, 0.3 and 0.5 MeV energies. Here, 0.1 MeV simulations are related to the recoil energy in Pu doping experiments where most of the structural damage comes from heavy recoils with approximately 0.1 MeV energy, whereas higher-energy events correspond to heavy ion bombardment experiments. We have simulated 0.1 MeV events with and without electronic energy loss, whereas for higher energy events, where a significant part of energy loss is due to electronic processes, the friction component was always on. For each simulation, we have simulated randomly chosen directions of the recoil (excluding low density) directions. The damage quantified below therefore refers to the average numbers and includes the standard deviation for each energy.

6.3 Results

We quantify damage production, evolution and recovery, and show the results in Fig. 6.1-6.2. As discussed in the previous chapters, we use N_{disp} and N_{def} to describe the damage creation and recovery. N_{disp} accounts for the total number of atoms that moved distance more than $d = 0.75$ Å from their initial position in the lattice. N_{def} is equal to the sum of vacancies and interstitial atoms in the system, identified using the sphere criterion for defect identification [29]. d should generally be smaller than half of the

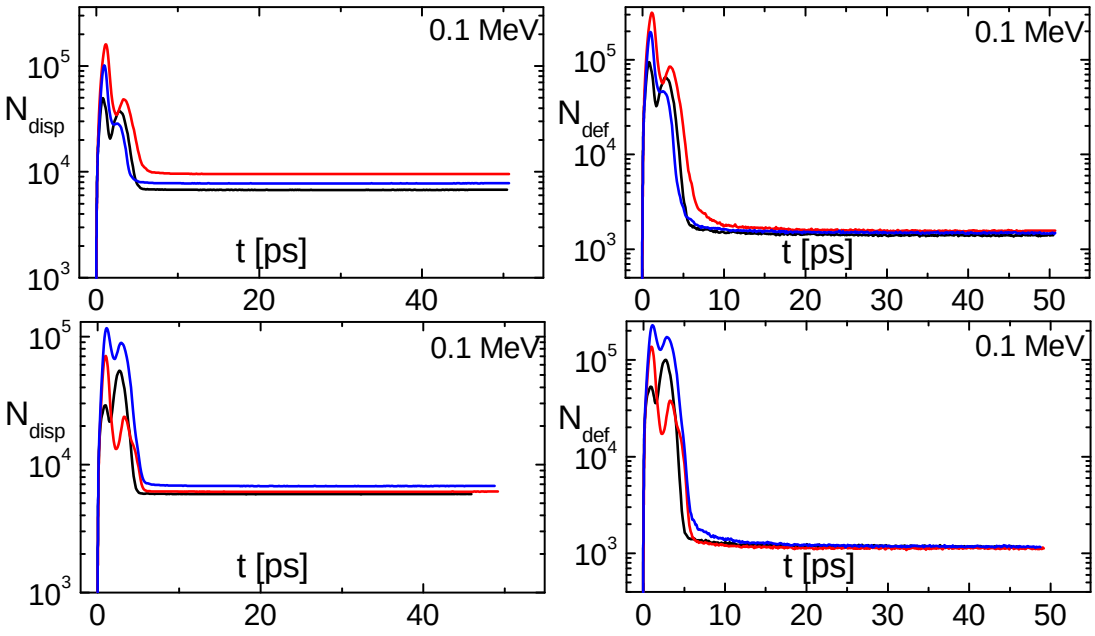

Figure 6.1: N_{disp} and N_{def} from 0.1 MeV knock-on atoms without (top) and 0.1 MeV knock-on atoms with the effect of electronic energy loss switched on (bottom) for three directions of the recoil.

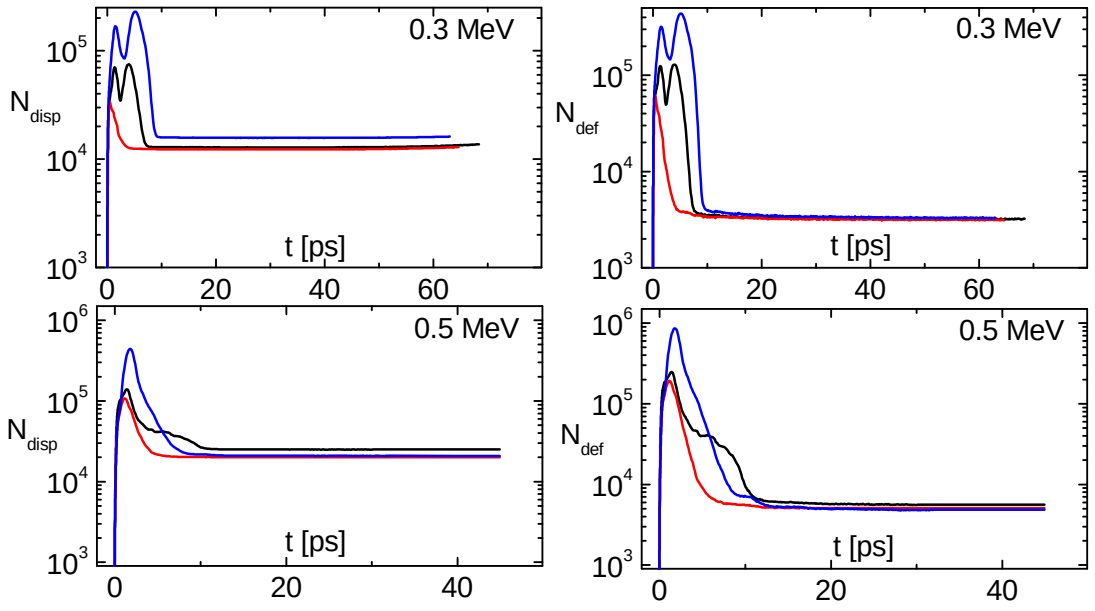

Figure 6.2: N_{disp} and N_{def} from 0.3 MeV knock-on atoms (top) and 0.5 MeV knock-on atoms (bottom) for three directions of the recoil.

	PEAK		END	
PKA energy	N_{disp}	N_{def}	N_{disp}	N_{def}
100 keV - no friction	104,000	192,000	8,000	1,500
	(32,000)	(72,000)	(800)	(50)
100 keV - friction	72,000	139,000	6,000	1,000
	(25,000)	(51,000)	(300)	(10)
300 keV - friction	113,000	209,000	14,000	3,000
	(60,000)	(116,000)	(1,000)	(50)
500 keV - friction	230,000	220,000	22,000	5,000
	(108,000)	(107,000)	(2,000)	(200)

Table 6-B: N_{disp} and N_{def}, calculated using the sphere criterion, at the peak of the damage (1-2 ps) and at the end of the simulation. Standard error of the mean is shown in the brackets calculated over three events.

closest interatomic separation, and is usually chosen not to account for typical thermal fluctuations of 0.2–0.3 Å. With a certain choice of d, N_{disp} and N_{def} can be compared and agree with other methods of defect identification such as Wigner-Seitz analysis [29, 30].

Fig. 6.1 shows N_{disp} and N_{def} for 100 keV cascades along different knock–on directions, without (top) and with (bottom) the friction term. Fig. 6.2 illustrates N_{disp} and N_{def} for 300 keV (top) and 500 keV (bottom) cascades respectively for different directions of the U recoil atom. We observe large peaks of both N_{disp} and N_{def} for all simulated cascades, followed by the marked decrease and saturation after about 5–10 ps of simulation time. Peak and final, long-time, values of N_{disp} and N_{def} are summarized in Table 6-B. We observe a substantial effect of the electronic friction on both N_{disp} and N_{def}, seen as a marked reduction of these numbers when the electronic friction is on. This effect originates from smaller energy available to produce both displaced atoms and surviving defects in the presence of electronic energy loss, and demonstrates the need to include electronic energy loss mechanisms in high-energy radiation damage simulations. Interestingly, we observed double peaks for cascades of 100 keV and 300 keV, which disappear for the higher energy cascades. This corresponds to the creation of

subcascades for the lower energy events and more continuous damage morphology for the higher energy cascades, as it was discussed in Chapter 3.

The physical origin of the large peaks is related to the deformation of the crystalline lattice around the collision cascade due to potential anharmonicity and associated expansion of the cascade structure, and was discussed in detail in Chapter 3. Here, we focus on the final values of $N_{\rm disp}$ and $N_{\rm def}$ at long times, and the latter in particular since it constitutes the final damage.

First, we observe large dynamic recovery of the induced damage, seen as the reduction of the final long-time $N_{\rm def}$ relative to $N_{\rm disp}$ in Figs. 6.1 - 6.2. The dynamic annealing is profound, and constitutes 80%–99% of damage recovery for different energies. This is consistent with earlier simulations of smaller energy of 30 keV [30], and is well illustrated in Figures 6.3–6.6 where we show both displaced and defect atoms for each simulated energy at various stages of damage propagation. In these figures, a typical cascade size, the maximal distance between defect atoms at the end of cascade propagation, is 600–1200 Å. In 8 out of the 12 cascade simulations the U recoil is not identified as a "defect".

The key to reconciling the exceptional radiation tolerance of ZrO_2 on experimental basis and the large number of defect atoms comes from realization that the final damage is very dilute, and mostly consists of isolated point defects and small disjoint clusters. In this case, X-ray probes, TEM and other non-local experimental probes do not detect amorphization as the loss of the long–range order, and hence consider zirconia as highly resistant despite the presence of the large number of local defects.

First, we support our proposal by the detailed analysis of defect atoms and the cascade morphology. In Table 6-C, we summarize how $N_{\rm def}$ partition in clusters of different sizes, and find that across all cascades simulated, 80-90% of $N_{\rm def}$ are isolated point defects, of which almost all (95–97 %) are O vacancies. In Fig. 6.7, we show the distribution of cluster sizes, and similarly find that most of the damage resides in isolated point

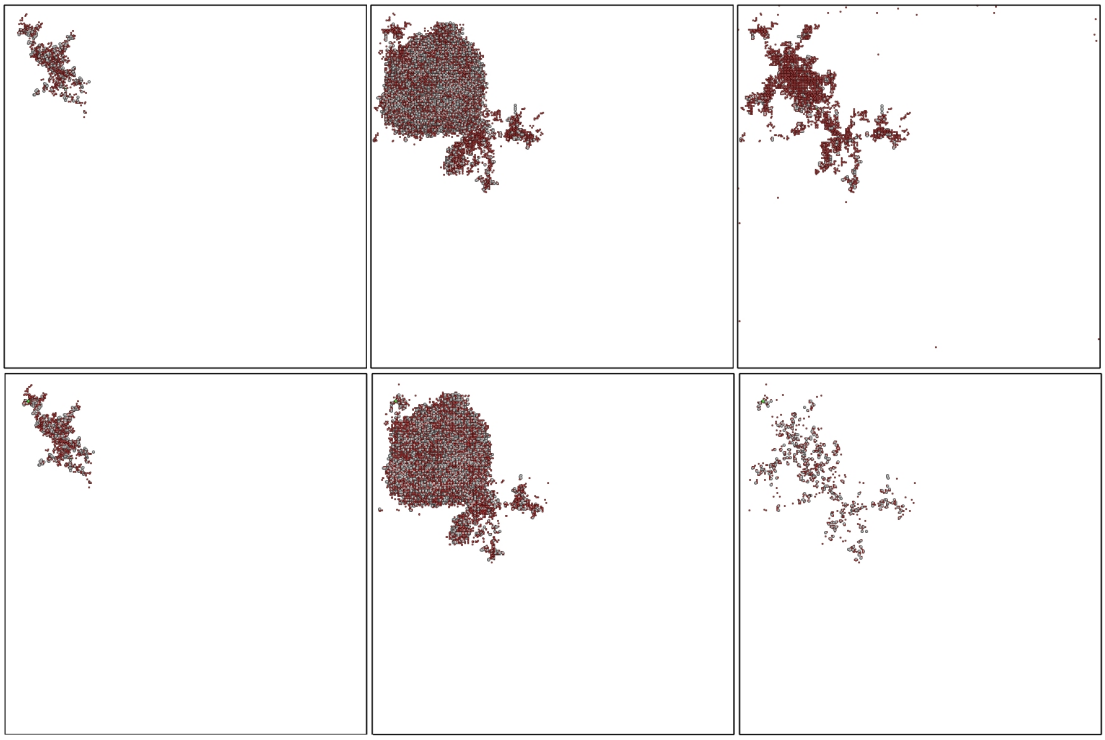

Figure 6.3: Time frames of displaced and defect atoms for different recoil energy cascades without the effect of electronic energy loss applied. The knock-on atom moves from the top left to the bottom right corner. Oxygen atoms are represented in red and zirconium atoms in grey. Top images represent the displaced atoms and the bottom images the defect atoms at 0.1 ps, 1.1 ps and 50 ps in a 0.1 MeV collision cascade in a system consisting of 20 million atoms. The simulation box length is about 645 Å and the cascade size (maximal separation between any two defect atoms in the cascade) is about 500 Å.

defects and small clusters. Notably, we find vacancy clusters to be appreciably larger than interstitial clusters (see Table 6-C and Fig. 6.7) making the damage dilute, the point to which we return below.

Second, we calculate the radial distribution function (RDF) over atoms in four simulated collision cascades. We calculate RDF as a histogram of separations between all atoms located within the sphere of radius R_{G} centered at $\mathbf{r}_{\mathrm{C}} = \sum \mathbf{r_i}/N$, where $\mathbf{r_i}$ are positions of the identified interstitial defect atoms i and N is their number. R_{G} is the radius of gyration of the collision cascade which we define as $R_{\mathrm{G}} = \sum \Delta\mathbf{r}/N$, where $\mathbf{\Delta r}$

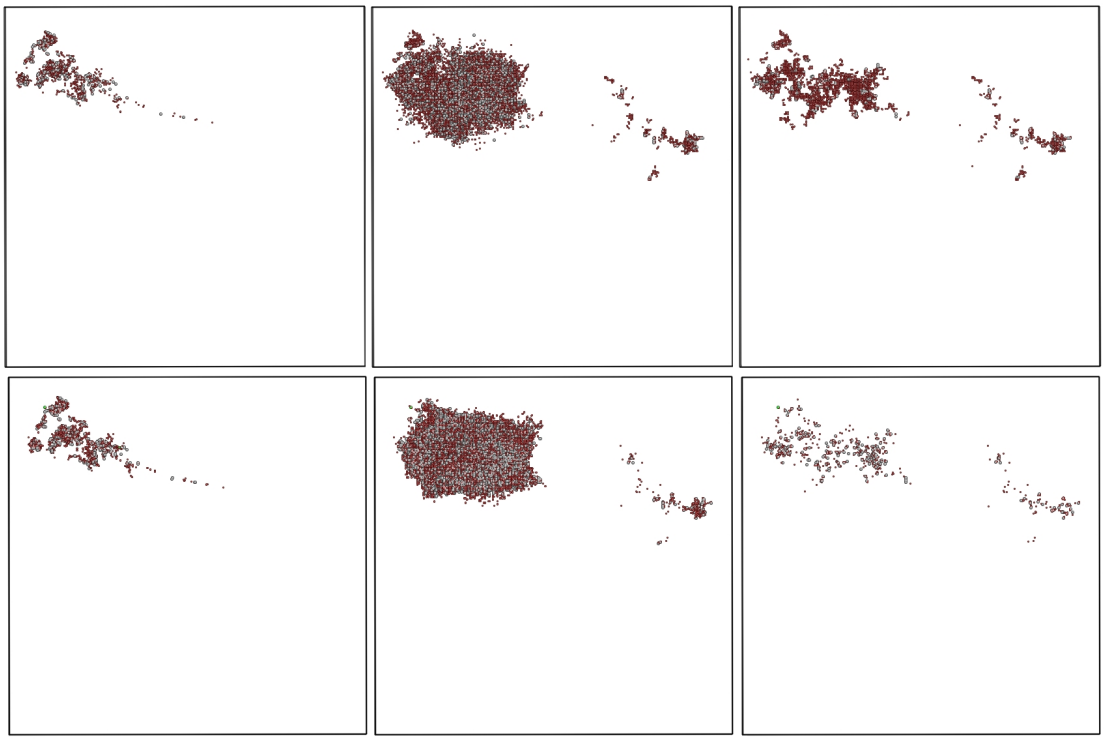

Figure 6.4: Time frames of displaced and defect atoms for different recoil energy cascades with the effect of electronic energy loss switched on. The knock-on atom moves from the top left to the bottom right corner. Oxygen atoms are represented in red and zirconium atoms in grey. Top images represent the displaced atoms and the bottom images the defect atoms at 0.1 ps, 1.1 ps and 50 ps in a 0.1 MeV collision cascade in a system consisting of 20 million atoms . The simulation box length is about 645 Å and the cascade size is about 600 Å.

is the distance between interstitials and the centre of gyration. In Fig. 6.8 we show $t(r) = g(r) \cdot r$, where $g(r)$ is normalized to value 1 for large distances, calculated over four simulated collision cascades, superimposed on the $t(r)$ calculated for the crystalline structure. The $t(r)$ for the crystalline and damaged structure coincide and for this we show the difference of $t(r)$ between the crystalline structure and four collision cascades in Figure 6.9 . Figures 6.8 and 6.9 show the near-identity of RDFs between the damaged and crystalline structure including, importantly, the presence of peaks beyond the short- and medium-range order. This is in contrast to the disappearance of peaks beyond the medium-range order in systems such as SiO_2, TiO_2, $ZrSiO_4$ and so on, where in-cascade

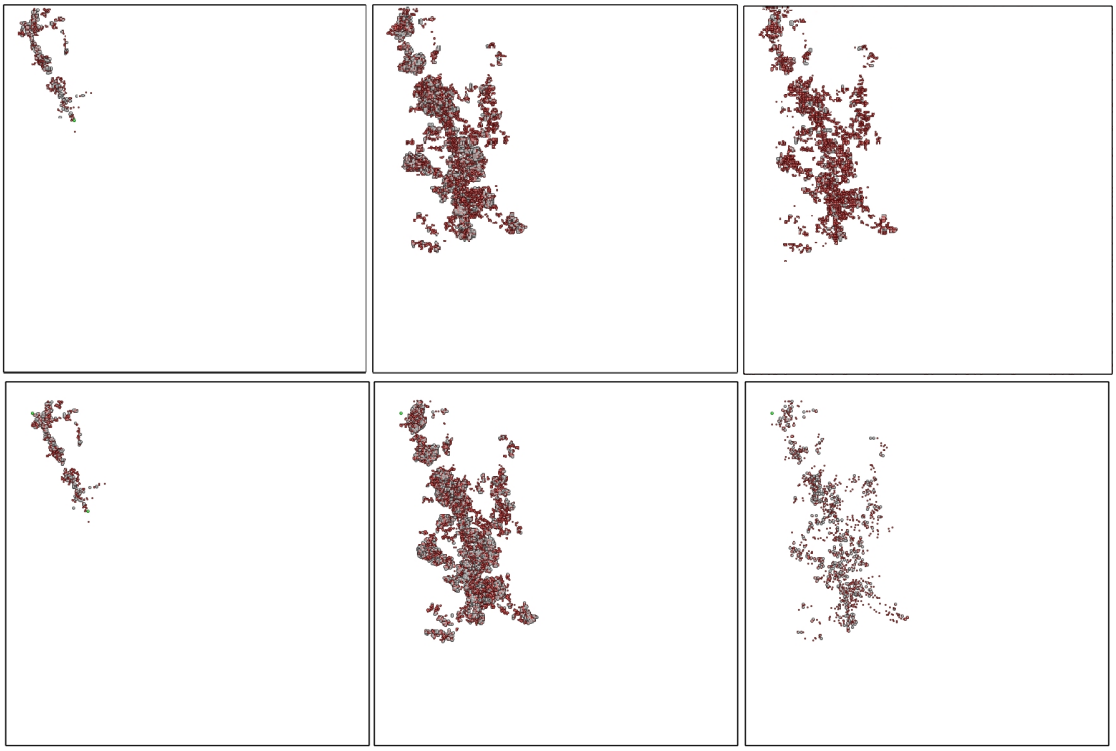

Figure 6.5: Time frames of displaced and defect atoms for different recoil energy cascades with the effect of electronic energy loss switched on. The knock-on atom moves from the top left to the bottom right corner. Oxygen atoms are represented in red and zirconium atoms in grey. Top images represent the displaced atoms and the bottom images the defect atoms at 0.1 ps, 0.45 ps and 64 ps for a 0.3 MeV collision cascade in a 70 million atoms system with box length of about 1000 Å. Cascade size is 800 Å.

amorphization is observed [31–35]. This all proves that despite the resistance revealed by long-range probes, the damage in ZrO_2 is substantial.

We now give more details about the nature of radiation damage in ZrO_2 presented in Table 6-C. We perform the analysis excluding vacancy-interstitial (V-I) pairs of the same species (both cation or both O) that lie within 3 Å of each other under the assumption that they will quickly annihilate with each other. The number of surviving defects increases with increasing energy. This increase is between square root dependence to linear dependence on energy.

The longest separation between defects in the cascade increases with increasing energy

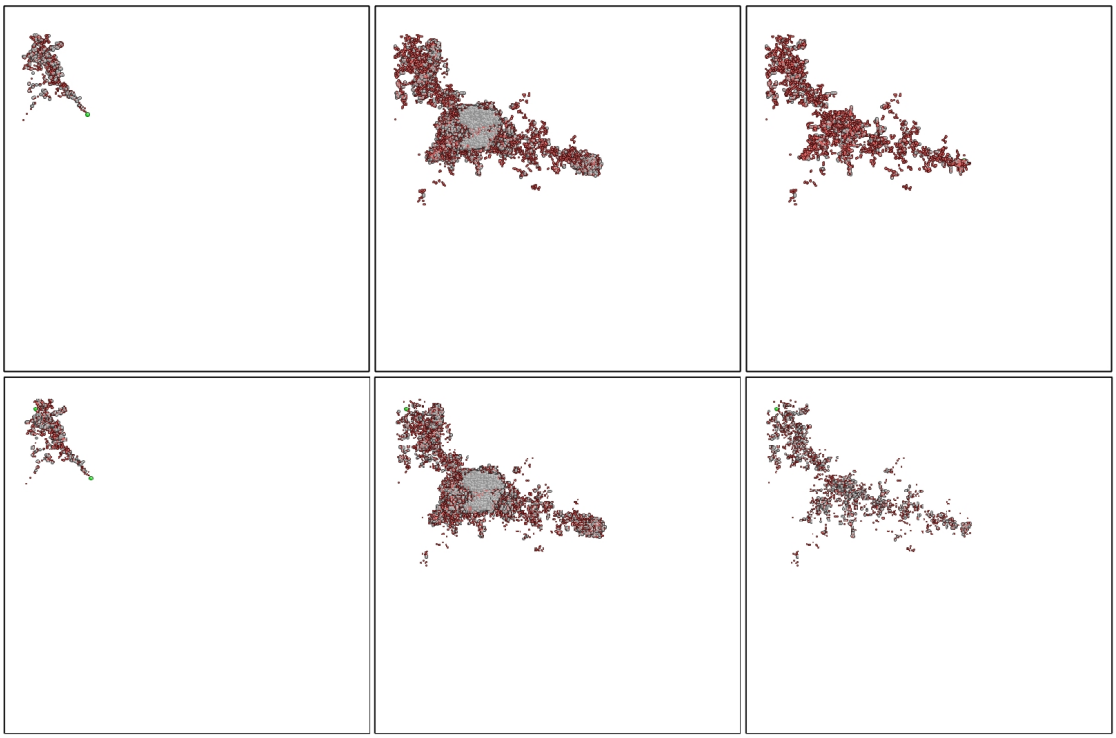

Figure 6.6: Time frames of displaced and defect atoms for different recoil energy cascades with the effect of electronic energy loss switched on. The knock-on atom moves from the top left to the bottom right corner. Oxygen atoms are represented in red and zirconium atoms in grey. Top images represent the displaced atoms and the bottom images the defect atoms at 0.1 ps, 1.2 ps and 17 ps for a 0.5 MeV collision cascade in a system of about 1300 Å length, consisting of 150 million atoms. Cascade size is 1200 Å.

and is also larger if no friction is applied, reflecting that including electronic stopping in high energy cascades results in smaller cascade size. This is also demonstrated by the radius of gyration at the end of the cascades, with values of 53, 91, 141, 210 Å averaged over three events for 100 keV cascades with electronic stopping, 100 keV cascades without the friction term applied, 300 keV and 500 keV cascades respectively. There is no obvious trend in the average distance between vacancies and nearest interstitials on the same sublattice with increasing energy or inclusion of friction. However, the Zr V-I separation is slightly larger than the O V-I separation, with the standard deviation of this distance being larger for the O sublattice. Therefore O defects can be found with large V-I separations. The fraction of oxygen atoms in vacancies and interstitials (calculated as

Property	**100keV friction**	**100keV no friction**	**300keV friction**	**500keV friction**
Zr interstitials (vacancies)	104 (1)	127 (7)	259 (5)	415 (25)
O interstitials (vacancies)	255 (7)	335 (14)	747 (6) (54)	1120
Fraction of O interstitials (vacancies)	0.7 (0.007)	0.7 (0.009)	0.7 (0.003)	0.7 (0.006)
Fraction of isolated interstitials	0.4 (0.01)	0.5 (0.02)	0.5 (0.006)	0.5 (0.003)
Fraction of isolated vacancies	0.3 (0.02)	0.3 (0.03)	0.4 (0)	0.3 (0.01)
Fraction of O in isolated interstitials	0.95 (0.007)	0.96 (0.009)	0.97 (0.003)	0.96 (0.007)
Fraction of O in isolated vacancies	0.92 (0.007)	0.93 (0.007)	0.94 (0.009)	0.94 (0.009)
Size of largest vacancy cluster	11 (1)	14 (4)	11 (0.3)	15 (1)
Size of largest interstitial cluster	4 (0.7)	3 (0.3)	3 (0.3)	3 (0.3)
Longest distance (Å) between defects	444 (71)	485 (38)	969 (70)	1227 (25)

Table 6-C: Defect analysis for different recoil energy cascades, for three different directions of the recoil. Standard error of the mean is shown in the brackets calculated over three events for each energy.

the fraction of the total number of well separated defects) is consistently 0.71 to 0.74 regardless of energy or friction. 30-38% of vacancies are isolated and this percent does not vary significantly with energy or friction. 44-49% of interstitials are isolated and again there is not much variation with energy or friction. Interstitials are more likely to be isolated than vacancies. Roughly one half of interstitials and one third of vacancies are isolated.

Consistent with the above, interstitial cluster sizes are smaller than vacancy cluster sizes. The largest interstitial cluster, consisting of both Zr and O, size is consistently

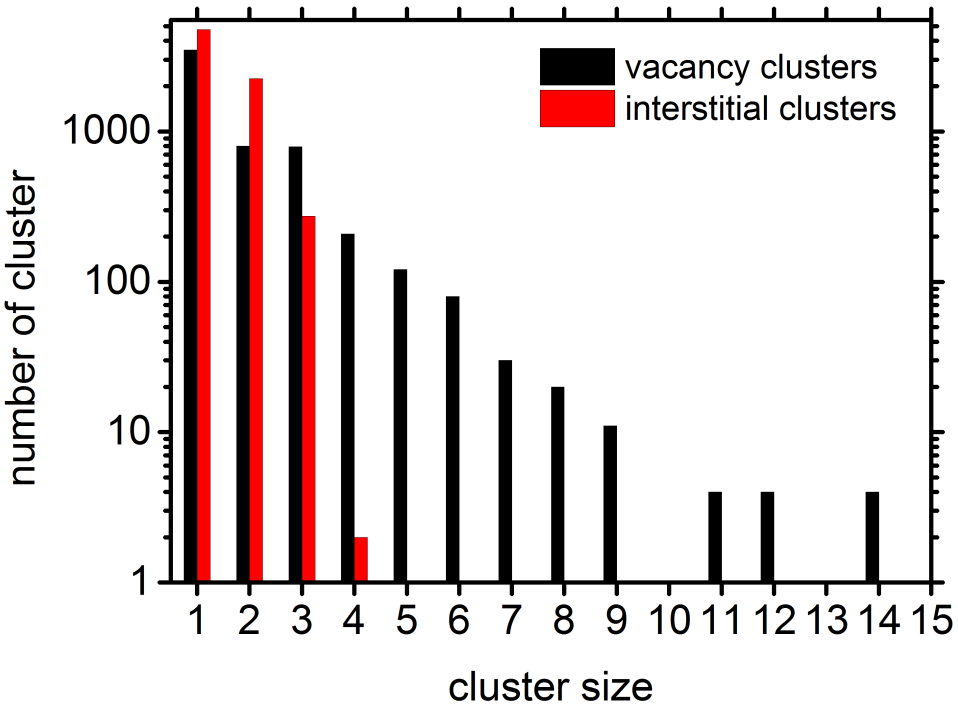

Figure 6.7: Distribution of cluster sizes for all cascades performed.

between 3 and 4 regardless of energy or friction. Vacancy clusters are larger and the size of the largest cluster increases with energy and also if friction is ignored. The largest vacancy cluster is between 11 and 21 vacancies. These vacancy clusters are either 50% O (Zr-O clusters) or fairly close to the stoichiometric ratio (O-Zr-O vacancy clusters). Fraction of oxygen among isolated vacancies is 0.92 to 0.94 and among isolated interstitials is 0.95 to 0.97. This seems independent of the energy and electronic stopping effect. Isolated defects are predominantly (almost entirely) on the oxygen sublattice.

Apart from elucidating the nature of high-energy radiation damage in zirconia and reconciling experimental and modeling results, our findings have an important implication for immobilization of nuclear waste. Even though zirconia does not amorphize in a sense of losing long-range order as most of the systems do [35], a large number of point defects and their clusters found here may play an important role in long-term evolution of the damage [36] and increased diffusion of radioactive species in particular. Especially

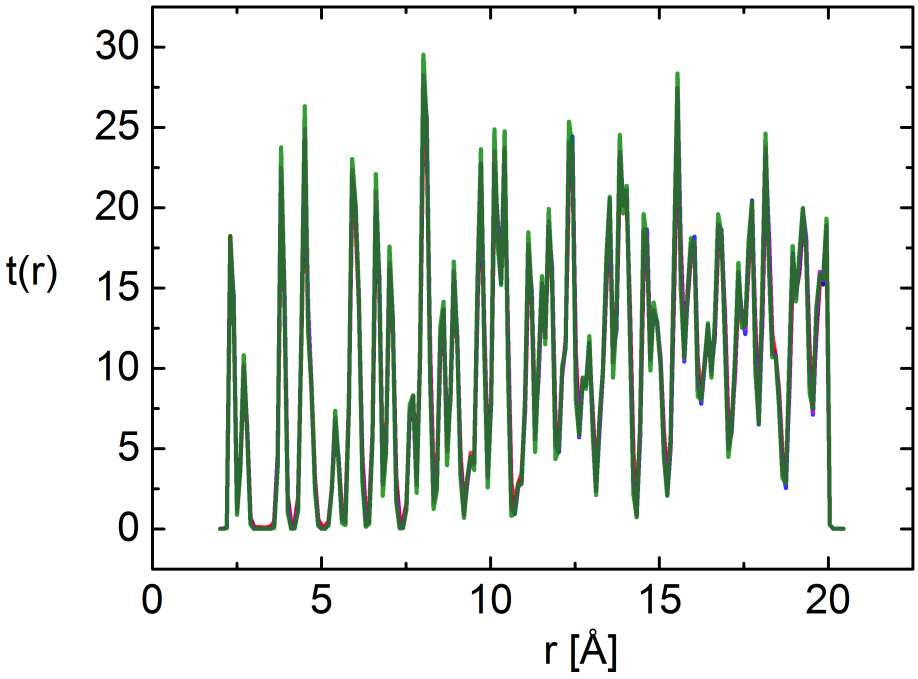

Figure 6.8: $t(r)$ calculated for for atoms in four simulated collision cascades and the crystalline lattice.

relevant in this context is the larger size of the vacancy clusters (10–15, see Table 6-C and Fig. 6.7) as compared to the size of interstitial clusters (3–4, see Table 6-C and Fig. 6.7). Consistent with experimental results [2, 6–8], these can provide fast diffusion pathways for encapsulated radioactive species, but also play a role in the nucleation and growth of bubbles affecting the overall performance of the waste form. Similar effects can be relevant in materials such as the widely used nuclear fuels UO_2 that are similar to zirconia in terms of structure and bonding.

6.4 Conclusions

In summary, we have found that a large number of point defects and their clusters co-exist with long-range structural coherence in irradiated zirconia. These defect structures are largely disjoint from each other and therefore represent a dilute damage that does

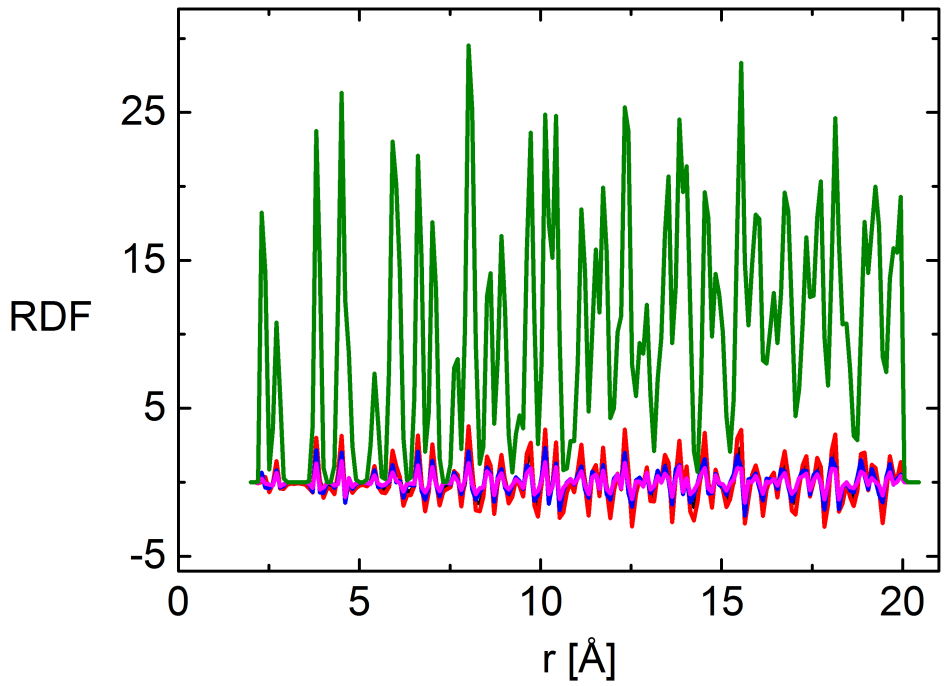

Figure 6.9: $t(r)$ calculated for the crystalline system and the differences between $t(r)$ for the crystalline structure and $t(r)$ for the damaged structures for four collision cascades.

not result in the loss of long-range structural coherence and amorphization. At the same time, long-time evolution of these defects may have important implications for using zirconia in intense radiation environments. This has implications for interpretation of other 'resistant systems', like $Gd_2Zr_2O_7$, $MgAlO_4$, Al_2O_3 and so on, and opens a new way of looking and understanding radiation damage in these systems.

References

[1] K. E. Sickafus, Hj. Matzke, Th. Hartmann, K. Yasuda, J.A. Valdez, P. Chodak III, M. Nastasi, and R.A. Verrall, J. Nucl. Mater. **274**, 66 (1999).

[2] K. E. Sickafus, Hj. Matzke, K. Yasuda, P. Chodak III, R. A. Verrall, P. G. Lucuta, H. R. Andrews, A. Turos, R. Fromknecht, and N. P. Baker, Nucl. Instr. Methods

Phys. Res. B **141**, 358 (1998).

[3] N. Yu, K. E. Sickafus, P. Kodali, and M. Nastasi, J. Nucl. Mater. **244**, 266 (1997).

[4] J.-M. Costantini, C. Trautmann, L. Thom, J. Jagielski, and F. Beuneu, J. Appl. Phys. **101**, 073501 (2007).

[5] J.-M. Costantini, F. Guillet, S. Lambert, D. Grbille, F. Beuneu, and C. Trautmann, J. Appl. Phys. **104**, 073504 (2008).

[6] N. Sasajima, T. Matsui, K. Hojou, S. Furuno, H. Otsu, K. Izui, and T. Muromura, Nucl. Instrum. Methods Phys. Res. B **141**, 478 (1998).

[7] Y. Zhang, W. Jiang, C. Wang, F. Namavar, P. D. Edmondson, Z. Zhu, F. Gao, J. Lian, and W. J. Weber, Phys. Rev. B **82**, 184105 (2010).

[8] J. Spino, H. Santa Cruz, R. Jovani-Abril, R. Birtcher, and C. Ferrero, J. Nucl. Mater. **422**, 27 (2012).

[9] K. Trachenko, M. Pruneda, E. Artacho and M. T. Dove, Phys. Rev. B, **70**, 134112 (2004).

[10] R. Devanathan, Nuclear Instr. Meth. Phys. Res. B **267**, 3017 (2009).

[11] B. E. Burakov, M. I. Ojovan and W. E. Lee, Crystalline Materials for Actinide Immobilization (Imperial College Press 2011).

[12] R.B. Heimann and T.T. Vandergraaf, J. Mater. Sci. Lett. **7**, 583 (1998).

[13] C. Degueldre and J.M. Paratte, Nucl. Technol. **123**, 21 (1998).

[14] W. J. Weber, R. C. Ewing, C. R. A. Catlow, T. Diaz de la Rubia, L. W. Hobbs, C. Kinoshita, Hj. Matzke, A. T. Motta, M. Nastasi, E. K. H. Salje, E. R. Vance and S. J. Zinklea, J. Mater. Res. **13**, 1434 (1998).

[15] G.R. Lumpkin, J. Nucl. Mater. **274**, 206 (1999).

[16] N. Nitani, K. Kuramoto, T. Yamashita, Y. Nihei, and Y. Kimura, J. Nucl. Mater. **319**, 102 (2003).

[17] M.A. Pouchon, M. Nakamura, Ch. Hellwig, F. Ingold, and C. Degueldre, J. Nucl. Mater. **319**, 37(2003).

[18] S. J. L. Billinge and Igor Levin, Science **316**, 561 (2007).

[19] I. T. Todorov, B. Smith, K. Trachenko and M. T. Dove, Capability Computing **6**, 12 (2005).

[20] I. T. Todorov, B. Smith, M. T. Dove and K. Trachenko, J. Mater. Chem. **16**, 1911

(2006).

[21] J. Yu, R. Devanathan and W. J. Weber, J. Mater. Chem **19**, 3923 (2009).

[22] A. M. Rutherford and D. M. Duffy, J. Phys.: Condens. Mat. **19**, 496201 (2007).

[23] A. Caro and M. Victoria, Phys. Rev. A **40**, 2287 (1989).

[24] J. M. Pruneda, D. Snchez-Portal, A. Arnau, J. I. Juaristi, and Emilio Artacho, Phys. Rev. Lett. **99**, 235501 (2007).

[25] E. Artacho, J. Phys. Condens. Matter, **19**, 275211 (2007).

[26] http://www.srim.org/

[27] J. F. Ziegler, J. P. Biersack and U. Littmark, *The Stopping and Range of Ions in Matter* (Pergamon, New York, 1985).

[28] K. Trachenko, M. T. Dove and E. K. H. Salje, J. Phys.: Condens. Matter, **15**, 6457 (2003).

[29] K. Nordlund, M. Ghaly, R. S. Averback, M. Caturla, T. Diaz de la Rubia and J. Tarus, Phys. Rev. B **57**, 7556 (1998).

[30] R. Devanathan, and W. J. Weber, J. Mater. Res. **23**, 593 (2008).

[31] I. Farnan, E. K. H. Salje, J. Appl. Phys. **89,** 2084 (2001).

[32] K. Trachenko, I. T. Todorov, M. T. Dove, E. Artacho and W. Smith, Phys. Rev. B **73** 174207 (2006).

[33] I. Farnan, H. Cho, W. J. Weber, Nature **445,** 190 (2007).

[34] K. Trachenko, M. T. Dove and E. K. H. Salje, Phys. Rev. B **65**, 180102(R) (2002).

[35] K. Trachenko, J. Phys. Condens. Matter **16**, 1491 (2004).

[36] X. M. Bai, A. F. Voter, R. G. Hoagland, M. Nastasi, B. P. Uberuaga, Science **327**, 1631 (2010).

Chapter 7

Summary

In this work we have performed large–scale simulations of radiation damage effects in materials for fusion applications and nuclear waste encapsulation. We have used MD methods, that give access to length and time scales that are not possible to access experimentally, and therefore they are an essential tool to provide fundamental understanding of phenomena at the atomistic level.

This work started with considerable development effort. New features and new capabilities were added to DLPOLY MD code, pushing the boundaries of what was believed to be possible in MD simulations. We faced new challenges, as it was the first time to simulate high–energy collision cascades, approaching more realistic energy and length scales. Working as a member of the DLPOLY developing team during the performance of these cascades led to useful alterations of the code, like modifications of existing routines and algorithms, that increase the code's efficiency and accuracy. These modifications will be useful not only for future radiation damage work, but also in other areas. Testing the capabilities of the code in these large scales and testing new features for radiation damage is important for a wider community interested in large-scale MD simulations. The updated version of the code includes the modifications made and the new features implemented for this research are being implemented in the next release of DLPOLY.

In this work we have simulated energies related to fusion, in the range of 1 MeV for the first time, obtaining a more realistic view of the phenomena that take place during high–energy irradiation of materials. The modeled systems had sizes up to 130 nm and contained up to 150 million atoms. These state-of-the-art simulations required up to 65,000 cores of HECToR, UK's National Supercomputing Facility, for one job. We have studied the creation, propagation and relaxation of high–energy collision cascades in materials for nuclear applications, the morphology of the cascade and the local defect structures. Systems of interest were bcc-iron, tungsten and cubic zirconia. Bcc-iron and tungsten are the main candidate materials for structural and plasma facing components of future fusion reactors. Cubic zirconia is a potential material for nuclear waste matrices, as it is one of the most resistant to amorphization ceramics. We approached radiation damage effects due to highly energetic particles in a more realistic way by taking into account the electronic effects. In high-energy collision cascades, most of the damage is due to the electronic effects; fast moving ions interact with the matter losing an important part of their energy due to electron scattering. We first introduced a friction term in the equation of motion to account for the electronic stopping, and then implemented the electron-phonon interactions in terms of an inhomogeneous Langevin thermostat.

The large scale analysis performed reveals information for the morphology of high–energy collision cascades, answering the question of *What does a high–energy collision cascade actually look like?* directly, rather than using extrapolations of previous results in lower energy cascades.

Specifically, we discussed the continuous morphology of high–energy collision cascades, which we found to be in contrast to the extrapolations of previous results obtained for lower energy cascades that were supporting the creation of subcascades even in higher energy events. This way, we emphasized the need to approach the multi-scale effects of the atomistic level, like radiation damage, in a more realistic way.

We observed defect structures in iron that have not been observed before. We took full account of the electronic effects for the first time in energies where these effects matter

the most. We found that the implementation of the electronic effects in high energy cascades can drastically change the cascade size and defect distribution into clusters. We emphasized that not only accurate interatomic potentials and high computation efficiency are necessary to model radiation damage, but also a local model to describe the electron-phonon coupling.

For the first time we implemented the electronic stopping mechanism in ionic materials in energies where the electronic energy loss is comparable to the nuclear energy loss. We found that the lack of amorphizability in zirconia co-exists with a large amount of dilute damage that does not result in the loss of long-range structural coherence and amorphization. We found that if electronic stopping is ignored, we may overestimate the ion range, the number of surviving defects, and the size of vacancy clusters.

Comparison between the electronic stopping mechanism and the full two-temperature model in high-energy cascade simulations in tungsten shows that if we ignore the electron phonon coupling we might overestimate the damage induced in the system. This highlights the need to take consideration of the electronic effects in high energy collision cascade simulations in metals. We also found that high temperature promotes damage recovery, resulting in less residual damage at the fusion reactor's operating temperature compared to simulations performed at room temperature. This work is on progress and will be finalized and published in full form shortly.

The reported point defect analysis can provide significant insights into the long–term evolution of the defects and their interaction with helium bubbles and transmutation gases, and predict how these interactions will affect the materials' performance. The outputs of our simulations can be used as input to long term analysis of defect evolution in other simulation methods, like Time Accelerated Dynamics.

This work is a first step towards the investigation of high-energy radiation effects in matter, in systems approaching the scale of micrometers. Development of better and more accurate interatomic potentials, improvement of the parallel computing architec-

ture as well as further development and improvement of the code scalability will allow researchers to gain insights into the interaction of high–energy radiation with matter. Further work can be performed by including in the simulations grain boundaries and interfaces, dislocations, doping the material under investigation, and studying the interactions with helium bubbles. Improved visualization methods of large scale simulations are also needed in order to have a closer look at phenomena that operate in the atomistic and mesoscopic scale.

In addition to nuclear industry applications, e.g. nuclear waste encapsulation and power plant structural materials, the methods and techniques used in this project are applicable to a wide field of interests, where matter is subject to intense irradiation. Examples of these fields are the semiconductor industry and space industry (e.g. space devices). This work is of cross-disciplinary importance, as there is a growing appetite for modeling of large systems approaching the micrometre scale. These state-of-the-art simulations are relevant to many interesting phenomena operating in the microscale, for example micro-structural changes, initiation of micro-cracks, interfacial effects, macromolecules and biological systems.

Importantly, large MD simulations not only can support the experiments, but can also be used to investigate processes that are difficult or impossible to be studied in the laboratory, for instance processes that take place in fusion or in space. Fundamental understanding of the processes and mechanisms that take place at the atomistic level is essential for predicting the materials' behaviour, improving their performance and maximizing their use. Further development and accomplishment of large-scale simulations will provide a detailed description of the microstructural evolution and resulting changes in the materials' properties that affect the materials' performance. Consequently, this will lead to deeper understanding of significant basic aspects of the interaction of radiation with solids, including radiation effects, defect investigation, ion-beam modification of materials, electronic and ionic transport, materials characterization, and in combination with experiments we will have a unique opportunity to make a substantial step

towards better development and use of materials.

Appendix A

Author's publications

A.0.1 Refereed Journal Publications

1. Trachenko, K.,**Zarkadoula, E.**, Todorov, I. T. , Dove, M. T., and Nordlund, K., "Modeling high-energy radiation damage in nuclear and fusion applications." *Nucl. Instr. Meth. Phys. Res. B*, 277 (15), 6–13, 2012.

2. **Zarkadoula, E.**, Daraszewicz, S. L., Duffy, D. M., Seaton, M., Todorov I. T., Dove, M. T, Nordlund, K., and Trachenko, K. "The nature of high-energy radiation damage in iron." *J. Phys.: Condens. Mat*, 25, 125402 2013
   IoP Select (http://iopscience.iop.org/0953-8984/labtalk-article/53397).

3. Andritsos, E. I., **Zarkadoula, E.**, Phillips, A. E., Dove, M. T., Walker, C. J., Brazhkin, V. V., and Trachenko, K., "Heat capacity of matter beyond the Dulong-Petit value" *J. Phys.: Condens. Matter*, 25, 235401, 2013
   IoP Select (http://iopscience.iop.org/0953-8984/labtalk-article/53517).

A.0.2 Submitted Journal Publications

1. **Zarkadoula, E.**, Daraszewicz, S. L., Duffy, D. M., Seaton, M., Todorov I. T.,

Dove, M. T, Nordlund, K., and Trachenko, K. “Electronic effects in high-energy radiation damage in iron.”

2. **Zarkadoula, E.**, Devanathan, R., Weber, W. J., Seaton, M., Todorov, I. T., Dove, M. T., and Trachenko, K. “Uncovering the hidden damage in irradiated zirconia.”

A.0.3 Papers under Preparation

3. **Zarkadoula, E.**, Daraszewicz, S. L., Duffy, D. M., Seaton, M., Todorov I. T., Dove, M. T, Nordlund, K., and Trachenko, K. “Modeling of high–energy radiation damage in tungsten.”